Statistics of energy dissipation rate and enstrophy in high-resolution direct numerical simulation of turbulence in a periodic box

Naoya Okamoto,[1,*] Takashi Ishihara,[2,†] Mitsuo Yokokawa,[3,‡] and Yukio Kaneda[4,§]

[1] *Center for General Education, Aichi Institute of Technology, Yakusa-cho, Toyota 470-0392, Japan*

[2] *Faculty of Environmental, Life, Natural Science and Technology, Okayama University, Okayama 700-8530, Japan*

[3] *Cyberscience Center, Tohoku University, Sendai 980-8579, Japan*

[4] *Graduate School of Mathematics, Nagoya University, Nagoya 464-8602, Japan*

(Received 30 August 2025; accepted 9 June 2026; published 16 July 2026)

We present a systematic analysis of the statistics of the energy dissipation rate ϵ and the enstrophy Ω, obtained from direct numerical simulations (DNS) of forced, incompressible turbulence in a periodic box at Taylor-scale Reynolds numbers up to $R_\lambda \approx 1740$. Both quantities, quadratic in the velocity-gradient tensor, are closely associated with small-scale intermittency. This paper considers the spectra of ϕ, the second-order correlation functions of ϕ, and the second-order moments of local averages of ϕ, where ϕ denotes ϵ, Ω, or their fluctuating components. The DNS results at $R_\lambda \approx 1100$–1740 reveal a wave-number range where the spectra scale with an exponent about $-2/3$ for both quantities. In physical space, the correlations and local averages show two scaling ranges: one with exponent about 0.23 for the total fields (ϵ and Ω) and another with exponent about 0.43 for their fluctuating parts. These ranges are close but not identical, and in both the correlation functions and the local averages, the total-field values are not dominated by the fluctuating parts. Under these conditions, the scaling exponents of the total and fluctuating components are unlikely to coincide, as the total includes a nonscaling mean contribution that is not negligible relative to the fluctuations. The results suggest that even at $R_\lambda \approx 1740$, the Reynolds number remains insufficient to reach the asymptotic regime assumed in intermittency theories.

DOI: 10.1103/xjtb-tt5g

I. INTRODUCTION

High-Reynolds-number (Re) turbulence exhibits strong intermittency at small scales. This feature is reflected in the statistics of the energy dissipation rate per unit mass, ϵ, defined as

$$\epsilon = \tfrac{1}{2}\nu(g_{\alpha\beta} + g_{\beta\alpha})(g_{\alpha\beta} + g_{\beta\alpha}), \tag{1}$$

where ν is the kinematic viscosity, $g_{\alpha\beta} = \partial u_\alpha/\partial x_\beta$ is the velocity gradient tensor, $\mathbf{u} = (u_1(\mathbf{x}, t), u_2(\mathbf{x}, t), u_3(\mathbf{x}, t))$ is the velocity at position $\mathbf{x} = (x_1, x_2, x_3)$ and time t, and the Einstein summation convention is used for repeated Greek indices. The statistics of ϵ serve as representative measures for characterizing small-scale intermittency in high-Re turbulence and have been the subject of extensive studies.

*Contact author: naoya@aitech.ac.jp
†Contact author: takashi_ishihara@okayama-u.ac.jp
‡Contact author: m.yokokawa@tohoku.ac.jp
§Contact author: kaneda@math.nagoya-u.ac.jp

Among the theoretical considerations concerning the statistics of ϵ, Kolmogorov's refinement (K62) [1] of his earlier similarity hypotheses is arguably the best known. Motivated by Landau's remarks on the random and intermittent nature of energy transfer from larger to smaller scales in high-Re turbulence, Kolmogorov proposed a refinement of his earlier similarity hypotheses (K41) [2]. As noted in the footnote of the original paper, this refinement is closely related to a lecture by Oboukhov [3].

In his refinement, Kolmogorov introduced the concept of the local energy dissipation rate,

$$\epsilon_r(\mathbf{x}, t) \equiv \frac{1}{V_r} \int_{|\mathbf{h}|<r} \epsilon(\mathbf{x}+\mathbf{h}, t) d\mathbf{h}, \tag{2}$$

which is defined as the spatial average of ϵ over a sphere of radius r centered at point $\mathbf{x}$. Here $V_r = \frac{4}{3}\pi r^3$ is the volume of the averaging sphere. He further assumed that for sufficiently large ratios L/r, the logarithm of $\epsilon_r(\mathbf{x}, t)$ follows a normal distribution with variance given by

$$\sigma_r^2(\mathbf{x}, t) = A(\mathbf{x}, t) + \mu \log(L/r), \tag{3}$$

where L is the external scale (i.e., the characteristic length scale of the energy-containing eddies), μ is a universal constant, and $A(\mathbf{x}, t)$ is a function determined by the macrostructure of the flow.

Various phenomenological models have been proposed to describe intermittency in turbulence, including Kolmogorov's refinement (K62), the β-model [4], multifractal models [5,6], and the She-Lévêque model [7] (see Frisch [8] for a review). These models are primarily concerned with the scaling properties of velocity increments or with general properties of coarse-grained energy dissipation.

Recently, we performed a series of high-resolution direct numerical simulations (DNS) of forced turbulent flows of an incompressible fluid in a periodic box, i.e., under periodic boundary conditions, with Taylor-scale Reynolds numbers up to $R_\lambda \approx 1740$. In this paper, we present DNS results concerning the two-point statistics of the energy dissipation rate ϵ and the enstrophy Ω. The enstrophy Ω, defined as $\Omega = \frac{1}{2}\omega^2$, is a non-negative quadratic quantity constructed from the velocity-gradient tensor and is strongly intermittent at small scales in high-Reynolds-number turbulence; here the vorticity vector is given by $\boldsymbol{\omega} = \boldsymbol{\nabla} \times \mathbf{u}$. In homogeneous turbulence, the mean values satisfy the relation $\langle\epsilon\rangle = \langle 2\nu\Omega\rangle$; however, in general their higher-order moments differ, for example $\langle\epsilon^p\rangle \neq \langle(2\nu\Omega)^p\rangle$ for $p \neq 1$, where angle brackets denote an appropriate statistical average. Since both ϵ and Ω are quadratic, non-negative local quantities constructed from the velocity-gradient tensor, it is of interest to examine their statistical properties in a unified manner. Among the various statistics that can be constructed from these quantities, we focus on those that are second order in ϵ and Ω for the following reasons:

(a) Statistics that are second order in ϵ or Ω correspond to fourth-order statistics in the velocity-gradient tensor $g_{\alpha\beta}$. Because the statistics of $g_{\alpha\beta}$ are generally non-Gaussian, the two-point second-order statistics of ϵ and Ω typically differ from those predicted under the assumption of multipoint Gaussianity of $g_{\alpha\beta}$. In this respect, these higher-order statistics can reveal the non-Gaussian nature of turbulence at small scales, unlike the first-order moments $\langle\epsilon\rangle$ and $\langle\Omega\rangle$, which depend only on second-order statistics of $g_{\alpha\beta}$.

(b) According to previous DNS studies, second-order statistics of ϵ or Ω are less sensitive to spatial and temporal resolution [9], as well as to arithmetic precision [10], compared with higher-order statistics. This implies that, given the limitations in resolution and arithmetic precision inherent in DNS, it is easier to obtain reliable data for these second-order statistics than for higher-order ones.

This paper considers (i) the spectra $E_\phi(k)$, (ii) the second-order correlation functions $C_\phi(r)$, and (iii) the second-order moments $\langle\phi_r^2\rangle$ of the local average ϕ_r (definitions are given in Sec. II B), where ϕ denotes either f or its fluctuating component $\tilde{f} \equiv f - \langle f\rangle$ and f denotes either ϵ or Ω. As will be shown in Sec. II, these quantities are not independent. In particular, the correlation functions $C_\phi(r)$ and the moments $\langle\phi_r^2\rangle$ can be expressed in terms of the spectrum $E_\phi(k)$. These quantities can therefore be determined once $E_\phi(k)$ is known.

Under mild assumptions, if the spectrum $E_\phi(k)$ follows a power law of the form

$$E_\phi(k) \propto k^{\mu_{k\phi}-1}, \tag{4}$$

in the inertial subrange $1/L \ll k \ll 1/\eta$, then the correlation $C_\phi(r)$ and the local average $\langle \phi_r^2 \rangle$ follow the power laws

$$C_\phi(r) \propto r^{-\mu_{C\phi}}, \tag{5}$$

$$\left\langle \phi_r^2 \right\rangle \propto r^{-\mu_\phi}, \tag{6}$$

in the inertial subrange $L \gg r \gg \eta$ and the exponents satisfy

$$\mu_{kf} = \mu_{k\tilde{f}} = \mu_{Cf} = \mu_{C\tilde{f}} = \mu_f = \mu_{\tilde{f}}, \tag{7}$$

for both $f = \epsilon$ and $f = \Omega$ (see Secs. II, III A, and III B). Here $\eta \equiv (\nu^3/\langle\epsilon\rangle)^{1/4}$ is the Kolmogorov microscale. The shift by -1 in the exponent of k in (4) is introduced because the Fourier transform of a power law $E_\phi(k) \propto k^{\mu-1}$ leads to $C_\phi(r) \propto r^{-\mu}$ under appropriate conditions.

According to K62 based on (3), the second-order moment of ϵ_r follows:

$$\left\langle \epsilon_r^2 \right\rangle \propto r^{-\mu}. \tag{8}$$

Thus the key parameter μ in (3), which characterizes the scale dependence of the statistics of ϵ_r in K62, can be related to the scaling exponent μ_ϵ of $\langle \epsilon_r^2 \rangle$. More generally, the exponents appearing in (4)–(6) characterize the scale dependence of statistical quantities associated with ϵ and Ω and may therefore be related to the strength of small-scale intermittency in high-Re turbulence. Considerable effort has been devoted to estimating such exponents in laboratory experiments and atmospheric and oceanic observations (see, e.g., Monin and Yaglom [11], Anselmet *et al.* [12], Sreenivasan and Kailasnath [13], Praskovsky and Oncley [14], and Cleve *et al.* [15] and references therein).

Because both ϵ and Ω involve velocity gradients in all three spatial directions, their measurement is generally difficult, or at least not straightforward, in experiments or in atmospheric and oceanic observations of high-Re turbulence. To address this challenge, surrogate quantities are often employed. For example, Anselmet *et al.* [12] and Sreenivasan and Kailasnath [13] used the surrogate $(\partial u/\partial t)^2$ for ϵ in their measurements, where u denotes the streamwise velocity fluctuation, while Praskovsky and Oncley [14] and Cleve *et al.* [15] adopted a different surrogate, $15\nu(\partial u_1/\partial x_1)^2$, in their study.

In contrast, computing ϵ and Ω in DNS is not particularly difficult, although still subject to certain limitations in numerical accuracy. As a result, DNS does not require the use of surrogate quantities. Moreover, DNS enables straightforward computation of averages over spherical geometries in both physical and wave-vector space. Consequently, there is no need to resort to surrogate procedures such as averaging over selected segments (e.g., lines) to estimate spherical averages. These advantages of DNS have facilitated detailed studies of the statistics of ϵ_r and Ω_r in turbulence (see, e.g., Iyer *et al.* [16], Lawson *et al.* [17], Yeung and Ravikumar [18], and Buaria and Sreenivasan [19] and references therein).

In the present work, we consider not only the second-order moments $\langle \phi_r^2 \rangle$ of the local averages, as in recent DNS studies [18,19], but also the spectra $E_\phi(k)$ and the correlation functions $C_\phi(r)$, on the basis of the DNS data described above, without resorting to surrogate quantities. For each of these statistics, we investigate whether there exists a range in which the quantity exhibits scaling behavior of the form (4)–(6) and, if so, estimate the corresponding scaling exponents.

The remainder of this paper is organized as follows. After a brief review of the DNS methods and turbulence characteristics, together with the definitions of the statistics analyzed in this paper and some of their basic relations, Sec. II presents numerical results for (i) the spectra of the energy dissipation rate, ϵ, and enstrophy, Ω; (ii) the two-point correlation functions of ϵ and Ω, as well as those of their fluctuating components; and (iii) the second-order moments of the local averages of ϵ and Ω, together with those of their fluctuating components. Section III discusses the differences among the intermittency-correction exponents obtained from the DNS data. Finally, Sec. IV summarizes the main results.

II. NUMERICAL RESULTS

A. Numerical methods and DNS parameters

The numerical methods used in the DNSs are essentially the same as those employed in our previous studies [20,21], which are briefly reviewed here for the reader's convenience. The turbulent velocity field is assumed to be 2π periodic in each of the Cartesian directions x, y, and z. A Fourier spectral method is employed. Aliasing errors are completely eliminated using a phase-shift technique, in which all Fourier modes satisfying $k > k_{\max} \equiv \sqrt{2}N/3$ are truncated, where k is the wave number and N is the number of grid points in each Cartesian direction in physical space. All simulations are carried out using double-precision arithmetic. The total energy, $E \equiv 3u'^2/2$, where u' is defined by $3(u')^2 = \langle u_1^2 + u_2^2 + u_3^2 \rangle$, is maintained at an approximately constant value ($\approx$0.5) by applying a form of forcing (negative viscosity) within the low-wave-number range $k < K_C$, where K_C(=2.5) is a constant.

Time integration is performed using a fourth-order Runge-Kutta method with a constant time step Δt, chosen such that $u'\Delta t/\Delta x < 0.1$, where $\Delta x = 2\pi/N$. The value 0.1 is an empirical choice based on our experience. If $[(u_1^2 + u_2^2 + u_3^2)^{1/2}]_{\max} = \alpha u'$, where $[\cdots]_{\max}$ denotes the maximum over all grid points and α denotes the corresponding nondimensional maximum for a given velocity field, then $C_U \equiv [(u_1^2 + u_2^2 + u_3^2)^{1/2}]_{\max} \Delta t/\Delta x = \alpha u' \Delta t/\Delta x$, so that the Courant number

$$C_A \equiv \Delta t \left[\frac{|u_1|}{\Delta x_1} + \frac{|u_2|}{\Delta x_2} + \frac{|u_3|}{\Delta x_3} \right]_{\max} \tag{9}$$

used in, e.g., Yeung and Pope [22] satisfies the inequality $C_A \leqslant \sqrt{3}C_U = \sqrt{3}\alpha u' \Delta t/\Delta x$, where Δx_i is the grid spacing in the ith Cartesian direction, and we have used $\Delta x_i = \Delta x$ in accordance with our DNS. The inequality $C_A \leqslant \sqrt{3}C_U$ is verified by noting $|u_1| + |u_2| + |u_3| \leqslant \sqrt{3}(u_1^2 + u_2^2 + u_3^2)^{1/2}$ for any (u_1, u_2, u_3). In our DNS, the largest observed value of α was about 7.4. For this value of α, the constraint $u'\Delta t/\Delta x < 0.1$ gives $C_U \lesssim 0.74$ and $C_A \lesssim 1.3$. These estimates are sufficiently small in view of the stability range of the fourth-order Runge-Kutta method associated with the convective term.

Table I summarizes the run conditions and representative turbulence characteristics. The number of grid points and the Reynolds number, $\mathrm{Re} \equiv u'L/\nu$, reach up to 16384^3 and 9.11×10^4, respectively. The largest-scale DNS was performed on the Fugaku supercomputer using 32 768 nodes. Fugaku consists of 158 976 nodes in total, and each node has 48 cores and 32 GiB of memory. The simulations were carried out using an in-house Message Passing Interface (MPI)-based Fortran code with an optimized Fastest Fourier Transform in the West (FFTW) library for large-scale parallel computations. The integral length scale L is defined as $L = \pi/(2u^2)\int E(k)/k dk$. The maximum Taylor microscale Reynolds number, R_λ, is 1736, where $R_\lambda \equiv u'\lambda/\nu$. The name of each run listed in the "I.C." column indicates the values of N and $k_{\max}\eta$. The initial condition for each run corresponds to the velocity field at the final time step of the run specified in the "I.C." column.

Our DNS series, listed in Table I, consists of two categories of runs. One, hereafter referred to as Group 1, comprises runs with $k_{\max}\eta \approx 1$, while the other, Group 2, comprises runs with $k_{\max}\eta \geqslant 2$. Even if r lies within the inertial range, it is natural to expect that the correlation function $C_\phi(r)$ and the local averages $\langle \phi_r^2 \rangle$ are dominated, or at least significantly influenced, by dissipation-range dynamics, where $\phi = \epsilon, \Omega, \tilde{\epsilon}$ or $\tilde{\Omega}$, each being second order in the velocity gradients. This consideration implies that reliable estimates of these statistics in general require that the high-wave-number modes be well resolved in the DNS. From this standpoint, only the runs in Group 2 are used in the following data analysis. The kinetic energy spectra of the runs of Group 2 are in good agreement, over the wave-number range $k\eta < 0.5$, with that of Group 1 reported in our previous study [20].

TABLE I. DNS conditions and turbulence characteristics at the final time step $t = t_F$. Runs 4096-1†, 6144-1†, and 8192-1† are not used in the analyses but are used to generate initial conditions for the other runs as indicated. Runs 2048-1 and 1024-2, with $(R_\lambda, t_F/T) = (732, 4.69)$ and $(268, 5.15)$, respectively, are taken from Ref. [15].

Run	I.C.	$\mathrm{Re}/10^4$	R_λ	$k_{\max}\eta$	$10^4\Delta t$	$10^5\nu$	$10^2\langle\epsilon\rangle$	L	$10^2\lambda$	$10^4\eta$	T	$10^2\tau_\eta$	t_F/T	t_F/t_η
4096-1†	2048-1	3.64	1136	1.0	2.50	1.73	7.46	1.09	3.41	5.13	1.89	1.52	2.44	303
6144-1†	4096-1†	6.36	1443	1.0	1.66	1.02	7.84	1.12	2.55	3.41	1.95	1.14	1.90	325
8192-1†	4096-1†	9.10	1728	1.0	1.25	0.7	7.97	1.10	2.10	2.56	1.91	0.94	1.24	252
2048-4	1024-2	0.250	283	4.0	1.5625	28	7.44	1.21	13.7	41.4	2.10	6.13	2.38	81.5
4096-2	2048-1	1.48	730	2.0	2.50	4.4	7.11	1.13	5.56	10.46	1.95	2.49	1.64	128
8192-2	4096-1†	3.64	1114	2.0	1.25	1.73	7.76	1.09	3.34	5.08	1.89	1.49	0.847	107
8192-4	2048-1	1.61	739	4.1	1.25	4.4	6.93	1.23	5.64	10.53	2.13	2.52	0.563	47.6
12288-2	6144-1†	6.36	1445	2.0	0.83	1.02	7.82	1.12	2.55	3.41	1.95	1.14	0.086	14.7
16384-2	8192-1†	9.11	1736	2.0	0.50	0.7	7.89	1.10	2.11	2.57	1.91	0.94	0.016	3.25
16384-4	8192-2	3.67	1101	3.9	0.50	1.73	7.94	1.10	3.30	5.05	1.91	1.48	0.008	1.03
16384-8	8192-4	1.60	740	8.1	0.50	4.4	6.90	1.22	5.64	10.54	2.12	2.52	0.005	0.42

As seen in Table I, the integration times t_F, normalized by the large-eddy turnover time $T(= L/u')$, are relatively short for runs in Group 2 compared with those in Group 1. For example, for Run16384-8, t_F is as short as $0.005T$ (approximately $0.42\tau_\eta$), where the Kolmogorov timescale is defined as $\tau_\eta \equiv (\nu/\langle\epsilon\rangle)^{1/2}$. It should be noted, however, that each run in Group 2 is a continuation of another, longer, run in Group 1, in the sense that, as indicated in Table I, the initial field of the former was generated—directly or indirectly—from the final field of the latter, which had been performed earlier with a similar Reynolds number, a simulation time of order T, and a lower resolution, $k_{\max}\eta \approx 1$. We have also confirmed that t_F is sufficiently long to be regarded as beyond the initial transient phase, in the sense that the rapid temporal variations in the high-wave-number ($k\eta > 1$) region of the energy spectrum $E(k)$, characteristic of the transient, become nearly negligible before t_F. This is consistent with the view that the characteristic timescales of small-scale statistics are much shorter than those of the largest eddies in three-dimensional turbulence. This view presumably underlies the multiresolution independent simulation technique employed in recent large-scale DNS studies by Yeung and Ravikumar [18] and by Yeung *et al.* [23]. As for the potential influence of the limited simulation time, see also the discussion in Sec. III B.

B. Statistics analyzed in this paper and basic relations

This section defines the statistical quantities analyzed in the present study to characterize small-scale intermittency and also reviews some basic relations among them. The focus is on second-order statistics constructed from the energy dissipation rate and the enstrophy, which are directly related to velocity-gradient fluctuations. In the following, the symbol ϕ denotes either f or its fluctuating component $\tilde{f} \equiv f - \langle f\rangle$, and f denotes either ϵ or Ω.

(i) Spectra $E_\phi(k)$

The spectrum $E_\phi(k)$ of ϕ is defined as

$$E_\phi(k) \equiv \int dS_k \widehat{C}_\phi(\mathbf{k}), \tag{10}$$

where $\widehat{C}_\phi(\mathbf{k})$ is the Fourier transform of the correlation function,

$$C_\phi(\mathbf{r}) \equiv \langle \phi(\mathbf{x}+\mathbf{r})\phi(\mathbf{x})\rangle, \tag{11}$$

given by

$$\widehat{C}_\phi(\mathbf{k}) = \frac{1}{(2\pi)^3}\int d\mathbf{r}\, C_\phi(\mathbf{r})\exp(-i\mathbf{k}\cdot\mathbf{r}). \tag{12}$$

This implies that $\langle\phi^2\rangle = \int_0^\infty E_\phi(k)dk$. Here the symbol $\int dS_k$ denotes integration over the spherical surface S_k of radius k, centered at $\mathbf{k}=\mathbf{0}$ in wave-vector space. We omit writing the position $\mathbf{x}$ on the left-hand side of Eq. (11), as $C_\phi(\mathbf{r})$ is independent of $\mathbf{x}$ in homogeneous turbulence. In this paper, we consider DNS of turbulence in a periodic box. In this case, C_ϕ is independent of $\mathbf{x}$ if the average $\langle\cdot\rangle$ is understood as including the spatial averaging over the periodic domain. Since $\langle f\rangle$ is independent of position, its Fourier transform vanishes except at $\mathbf{k}=\mathbf{0}$. Therefore, $\widehat{f}(\mathbf{k}) = \widehat{\tilde{f}}(\mathbf{k})$, and $E_f(k) = E_{\tilde{f}}(k)$ for $k \neq 0$.

(ii) Second-order correlation functions $C_\phi(r)$

The spherically averaged second-order correlation function is defined as

$$C_\phi(r) \equiv \frac{1}{4\pi r^2}\int dS_r\, C_\phi(\mathbf{r}), \tag{13}$$

where $\int dS_r$ denotes the integral over the spherical surface S_r of radius r, centered at $\mathbf{r}=0$ in physical space. If $C_\phi(\mathbf{r})$ is isotropic (i.e., independent of the direction $\mathbf{r}/r$), then $C_\phi(r) = C_\phi(\mathbf{r})$ for any direction $\mathbf{r}/r$. Using the decomposition $f = \langle f\rangle + \tilde{f}$ and the identity $\langle\tilde{f}\rangle = 0$, it follows that

$$C_f(\mathbf{r}) = \langle f\rangle^2 + C_{\tilde{f}}(\mathbf{r}), \tag{14}$$

and, hence,

$$C_f(r) = \langle f\rangle^2 + C_{\tilde{f}}(r). \tag{15}$$

(iii) Second-order moments $\langle{\phi_r}^2\rangle$ of the local average ϕ_r

The local average ϕ_r is defined as in Eq. (2), with ϕ in place of ϵ. It can be shown that

$$\langle f_r\rangle = \langle f\rangle, \quad \langle\widetilde{f_r}\rangle = 0, \quad \left\langle\widetilde{f_r}^2\right\rangle \geqslant 0, \tag{16}$$

and therefore

$$\left\langle{f_r}^2\right\rangle = \langle f\rangle^2 + \left\langle\widetilde{f_r}^2\right\rangle \geqslant \langle f\rangle^2. \tag{17}$$

C. Spectra of squared energy dissipation and squared enstrophy

Let

$$\phi(\mathbf{x}) = \sum_{\boldsymbol{k}}\hat{\phi}(\mathbf{k})\exp(i\mathbf{k}\cdot\mathbf{x}) \tag{18}$$

be the Fourier expansion of $\phi(\mathbf{x})$ in a periodic box of turbulence with fundamental periodicity length 2π in each Cartesian direction, where the sum is taken over all integer wave vectors $\mathbf{k} = (k_1,k_2,k_3)$. Then we have

$$\langle\phi(\mathbf{x})\phi(\mathbf{x}+\mathbf{r})\rangle_V = \sum_{\mathbf{k}}\hat{\phi}(\mathbf{k})\hat{\phi}(-\mathbf{k})\exp(i\mathbf{k}\cdot\mathbf{r}), \tag{19}$$

where the brackets $\langle\cdots\rangle_V$ denote spatial averaging over $\mathbf{x}$ within the fundamental periodic domain. In deriving this, we have used the identity $\langle\exp[i(\mathbf{k}+\mathbf{k}')\cdot\mathbf{x}]\rangle_V = \delta_{\mathbf{k}+\mathbf{k}'}$, where $\delta_{\mathbf{q}} = 1$ if $\mathbf{q}=\mathbf{0}$, and 0 otherwise. This implies that the function $\widehat{C}_\phi(\mathbf{k})$ in (12) is given by

$$\widehat{C}_\phi(\mathbf{k}) = \langle\hat{\phi}(\mathbf{k})\hat{\phi}(-\mathbf{k})\rangle_e, \tag{20}$$

where the average $\langle\cdots\rangle$ is to be understood as $\langle\cdots\rangle = \langle\langle\cdots\rangle_V\rangle_e$, with $\langle\cdots\rangle_e$ denoting the ensemble average.

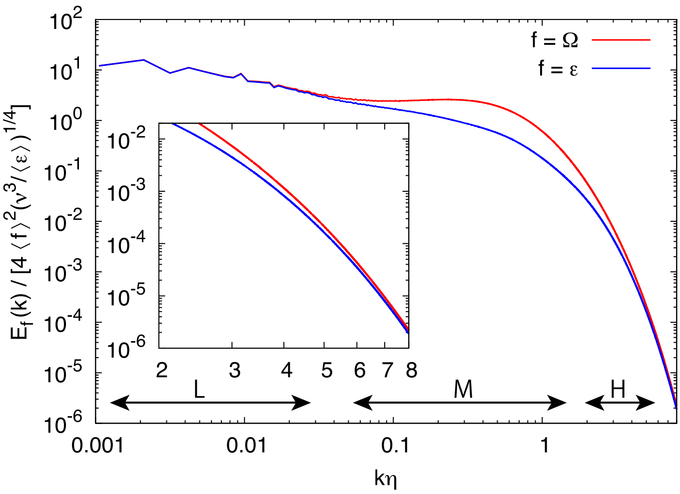

FIG. 1. Spectra $E_\epsilon(k)$ and $E_\Omega(k)$ from Run16384-8 ($R_\lambda \approx 740$, $k_{\max}\eta \approx 8$). Inset shows a zoom-in of the spectra at $k\eta > 2$.

When computing $E_\phi(k)$ as defined in (10), we assume that the surface integral $\int dS_k$ over S_k (for $k = 1, 2, 3, \ldots$) can be approximated by averaging over a spherical shell of thin width δ, such that $k - \delta/2 \leqslant |\mathbf{k}| < k + \delta/2$, with $k = 1, 2, 3, \ldots$. All the figures presented below are based on computations with $\delta = 1$.

In general, the ensemble average $\langle \cdots \rangle_e$ depends on the number of realizations, and it is desirable to make the integration time T_S as long as possible and to perform as many realizations as feasible. However, this is prohibitively expensive in DNS with very large N. Since the number of nodes within each spherical shell increases with k, we assume that the computed $E_\phi(k)$ is not highly sensitive to the number of realizations for sufficiently large k, which is the range of primary interest in this study. We therefore compute statistics solely from the velocity field at the final time t_f in the following analysis. This assumption implies that we may set $\langle f \rangle_V = \langle f \rangle$, i.e.,

$$\langle \tilde{f}(\mathbf{x}) \rangle_V = \langle f(\mathbf{x}) - \langle f \rangle \rangle_V = 0. \tag{21}$$

Then (18) yields $\widehat{\tilde{f}}(\mathbf{0}) = 0$.

In view of the relations (18), (20), and $f(\mathbf{x}) = \langle f \rangle + \tilde{f}(\mathbf{x})$, where $\langle f \rangle$ is independent of $\mathbf{x}$, it is shown that

$$\widehat{C}_f(\mathbf{k}) = \widehat{C}_{\tilde{f}}(\mathbf{k}) + \langle f \rangle^2 \delta_{\mathbf{k}}, \tag{22}$$

where if $\widehat{\tilde{f}}(\mathbf{0}) = 0$ as noted above, $\widehat{C}_{\tilde{f}}(\mathbf{0}) = 0$.

Figure 1 shows the spectra $E_\epsilon(k)$ and $E_\Omega(k)$, computed as described above, plotted against $k\eta$ for $k = 1, 2, 3, \ldots, k_{\max} - 1$ in Run16384-8 ($R_\lambda \approx 740$, $k_{\max}\eta \approx 8$). According to a simple dimensional analysis based on K41, the spectra $E_f(k)$ may be expressed as

$$E_f(k) = \langle f \rangle^2 \eta G(k\eta) = \langle f \rangle^2 \left(\frac{\nu^3}{\langle \epsilon \rangle} \right)^{1/4} G(k\eta), \tag{23}$$

in the range $kL \gg 1$, where $G(k\eta)$ is a nondimensional function of $k\eta$. We therefore plot $E_f(k)$ normalized by $4\langle f \rangle^2/(\nu^3/\langle \epsilon \rangle)^{1/4}$. A factor of 4 is introduced to facilitate comparison with the plots in our previous report [24]. In view of (22), which implies that $\hat{C}_f(\mathbf{k}) = \hat{C}_{\tilde{f}}(\mathbf{k})$ for all $\mathbf{k} \neq \mathbf{0}$, we have $E_{\tilde{f}}(k) = E_f(k)$ for $k \geqslant 1$ under the present approximation used in computing $E_\phi(k)$ from $\hat{C}_\phi(\mathbf{k})$. Accordingly, we omit plotting $E_{\tilde{f}}(k)$.

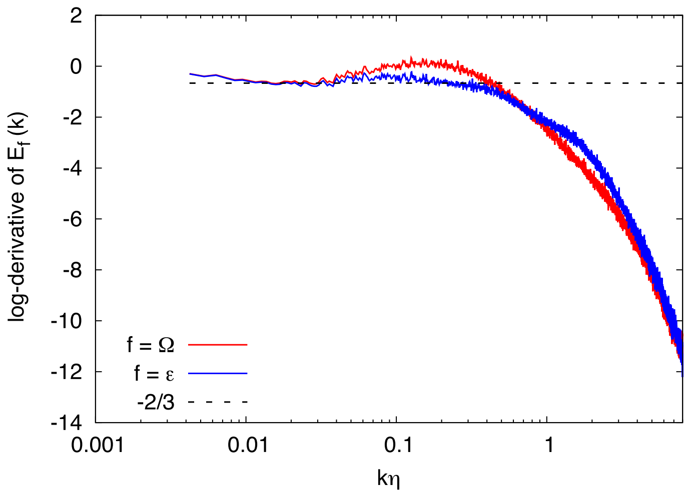

FIG. 2. Five-point averages $\xi^5_{\Phi,k}(k)$ of the logarithmic derivatives for (a) $\Phi(k) = E_\epsilon(k)$ and (b) $\Phi(k) = E_\Omega(k)$ in Fig. 1 vs $k\eta$.

As seen in Fig. 1, in the low-wave-number range $k < k_\ell$ with $k_\ell \eta \approx 0.01$ [marked as "L (low)"], $E_\epsilon(k)$ and $E_\Omega(k)$ are nearly identical. In contrast, in the region around $k\eta \approx 1$ [marked as "M (middle)"], $E_\Omega(k)$ exceeds $E_\epsilon(k)$, and the two spectra differ significantly.

These characteristics observed in Fig. 1 are consistent with those shown in Fig. 1 of our previous report [24]. The latter was obtained from DNS with $k_{\max}\eta \approx 1$, while the former is based on DNS with a much larger $k_{\max}\eta$ (approximately 8). In this sense, the present result may be regarded as an updated extension of the earlier one. Owing to the increased resolution (i.e., larger $k_{\max}\eta$), we are now able to observe $E_\epsilon(k)$ and $E_\Omega(k)$ in the higher-wave-number range $k\eta > 1$ (up to $k\eta < 8$). As seen in Fig. 1, the two spectra are nearly indistinguishable in the range $k\eta \gtrsim 2$, marked as "H (high)." One might therefore think that the two spectra coincide at sufficiently large k, for example for $k\eta > 3$. However, closer inspection reveals that this is not the case, as shown in the inset of Fig. 1.

This is confirmed by Fig. 2, which shows the logarithmic derivative defined as

$$\xi_{\Phi,k}(k) \equiv \frac{d \log \Phi(k)}{d \log k} \tag{24}$$

for $\Phi(k) = E_f(k)$ with $f = \epsilon$ or $f = \Omega$. To reduce noise, Fig. 2 plots the five-point moving average of the logarithmic derivative, defined by $\xi^5_{\Phi,k}(k) \equiv [\xi_{\Phi,k}(k+2) + \xi_{\Phi,k}(k+1) + \xi_{\Phi,k}(k) + \xi_{\Phi,k}(k-1) + \xi_{\Phi,k}(k-2)]/5$ rather than $\xi_{\Phi,k}(k)$ itself.

Figures 3(a) and 3(b) respectively show collections of the spectra $E_\epsilon(k)$ and $E_\Omega(k)$ plotted against $k\eta$ for the runs (with $k_{\max}\eta \geqslant 2$) listed in Table I. Correspondingly, Figs. 4(a) and 4(b) present the logarithmic derivatives $\xi_{E_\epsilon,k}(k)$ and $\xi_{E_\Omega,k}(k)$, respectively. Unlike Figs. 1 and 2, the spectra and the logarithmic derivatives in Figs. 3 and 4 are not limited to those by Run16384-8($R_\lambda \approx 740$). It is seen in Figs. 3(a) and 4(a) that the spectrum $E_\epsilon(k)$ in a certain wave-number range, denoted as I_D, around $k\eta \approx 0.01$ is not so much sensitive to $k_{\max}\eta$ and R_λ in "high-R_λ DNSs," at least in the cases considered here. Here we refer to DNS runs with $R_\lambda > 1100$ as "high-R_λ DNSs" to distinguish them from those at lower R_λ.

According to Figs. 3(a) and 4(a), the spectrum $E_\epsilon(k)$ in high-R_λ DNS fits well to a local power law such that

$$E_\epsilon(k) \propto k^{\mu_{k\epsilon}-1}, \quad (\mu_{k\epsilon} \approx 1/3). \tag{25}$$

in I_D.

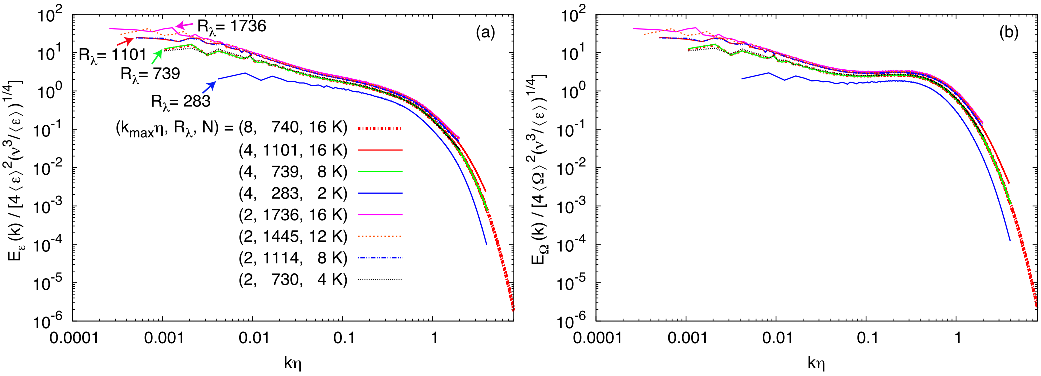

FIG. 3. Spectra $E_\epsilon(k)$ and $E_\Omega(k)$ by the runs listed in Table I, (a) $E_\epsilon(k)$ vs $k\eta$ and (b) $E_\Omega(k)$ vs $k\eta$.

A similar tendency is observed in the spectra $E_\Omega(k)$ shown in Figs. 3(b) and 4(b). In the high-R_λ DNSs, $E_\Omega(k)$ fits well to a local power law such that

$$E_\Omega(k) \propto k^{\mu_{k\Omega}-1}, \quad (\mu_{k\Omega} \approx 1/3), \tag{26}$$

in a wave-number range, denoted as I_Z, located around $k\eta \approx 0.01$ or equivalently $kL \approx 30$. Although the ranges I_D and I_Z are not exactly the same, they are relatively close to each other. In (25) and (26), the exponents are written as $\mu_{k\epsilon} - 1$ and $\mu_{k\Omega} - 1$—rather than simply $-\mu_{k\epsilon}$ and $-\mu_{k\Omega}$—in view of (4) and (7).

Figures 5(a) and 5(b) present the same spectra as Figs. 3(a) and 3(b), respectively, but plotted with a linear scale on the horizontal axis. In the dissipation range—approximately for $k\eta > 1$—both $E_\epsilon(k)$ and $E_\Omega(k)$ exhibit a rapid decay with increasing $k\eta$. This decay appears to be closer to exponential, i.e., $\log \Phi(k) \propto -k$, than Gaussian, i.e., $\log \Phi(k) \propto -k^2$, where $\Phi(k)$ denotes either $E_\epsilon(k)$ or $E_\Omega(k)$. A similar approximately exponential decay has been observed in the energy spectrum $E(k)$ (see, e.g., the review by Kaneda and Morishita [25], Khurshid *et al.* [26], Buaria and Sreenivasan [27], and references therein).

Notably, at $k\eta \gtrsim 3$, the spectra from Run 16384-8 ($k_{max}\eta \approx 8$) exhibit a slight concavity. If $\Phi(k)$ is approximated among various possibilities by a stretched exponential of the form $\log \Phi(k) \propto -k^{\alpha_\Phi}$, then this behavior suggests that the exponent α_Φ is close to unity but slightly smaller. It would be of interest to investigate the k and Re dependencies of $E_\epsilon(k)$ and $E_\Omega(k)$ in more detail, like in previous studies on the energy spectrum $E(k)$ (see the references noted above).

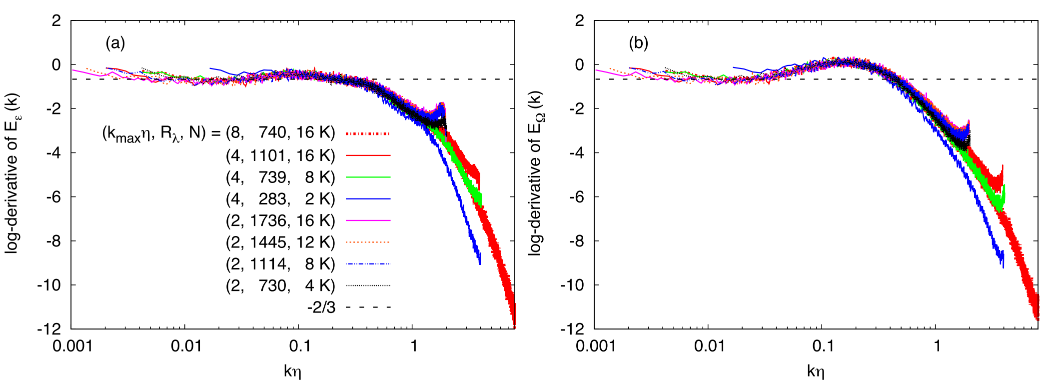

FIG. 4. Logarithmic derivatives of spectra (a) $E_\epsilon(k)$ and (b) $E_\Omega(k)$ in the runs listed in Table I vs $k\eta$.

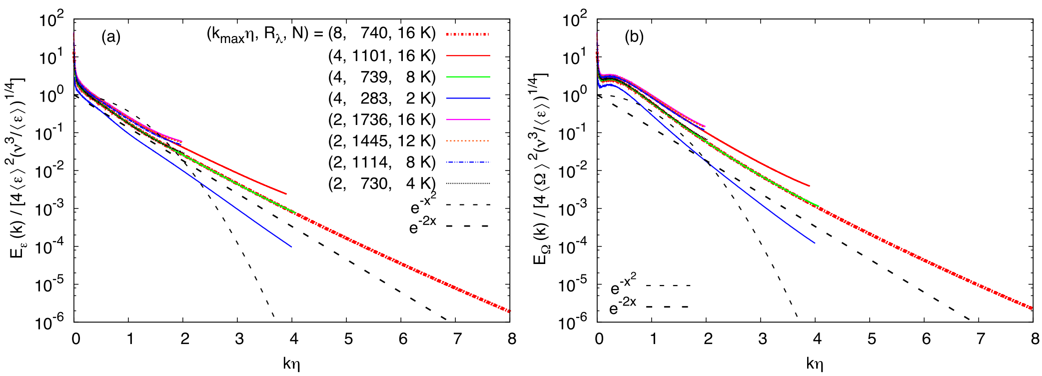

FIG. 5. The same as Figs. 3(a) and 3(b) but using a linear scale on the horizontal axis. The colored lines have the same meaning as in Fig. 3.

In contrast to $E_\epsilon(k)$ shown in Fig. 3(a), the spectrum $E_\Omega(k)$ in Fig. 3(b) exhibits a noticeable bump, located around $k\eta \approx 0.1$. Figure 6 plots the location and height of this peak, denoted by (k_p, Z_p), in the (k, E_Ω) plane against the Taylor-scale Reynolds number R_λ. The peak wave number k_p shows only a weak dependence on R_λ, whereas the peak height Z_p increases with R_λ for the DNS considered.

D. Two-point correlation functions

In terms of the Fourier transform $\widehat{C}_\phi(\mathbf{k})$ of $C_\phi(\mathbf{r})$, one can express $C_\phi(\mathbf{r})$ as

$$C_\phi(\mathbf{r}) = \int d\mathbf{k}\, \widehat{C}_\phi(\mathbf{k}) \exp(i\mathbf{k}\cdot\mathbf{r}) = \int_0^\infty dk \int dS_k\, \widehat{C}_\phi(\mathbf{k}) \exp(i\mathbf{k}\cdot\mathbf{r}), \tag{27}$$

where we have used the identity $\int d\mathbf{k} = \int_0^\infty dk \int dS_k$, with dS_k denoting the surface element over the shell of constant $|\mathbf{k}| = k$. The spherically averaged correlation function $C_\phi(r)$ is given by

$$C_\phi(r) = \int_0^\infty dk\, E_\phi(k) \frac{\sin(kr)}{kr} \tag{28}$$

(see the Appendix for the derivation).

Figures 7(a) and 7(b) show the correlation functions $C_\epsilon(r)$ and $C_{\tilde{\epsilon}}(r)$, respectively, normalized by $\langle\epsilon\rangle^2$, plotted against r/η. The function $C_{\tilde{\epsilon}}(r)$ was computed using (28), with $E_{\tilde{\epsilon}}(0) = 0$ and the

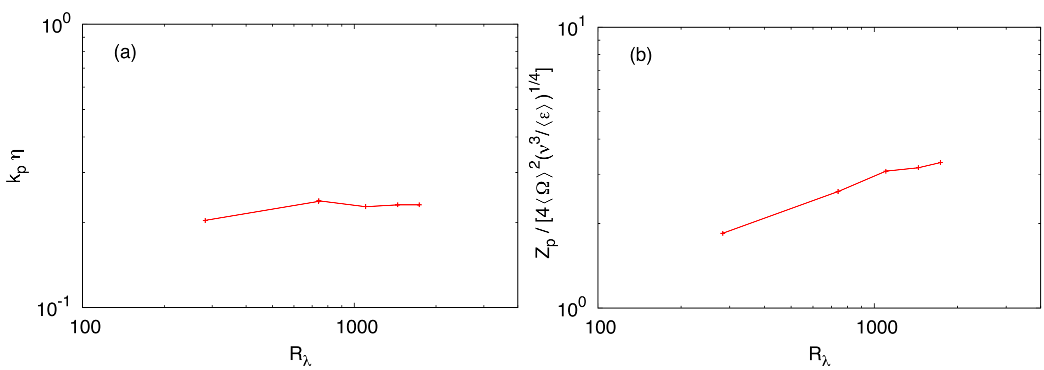

FIG. 6. Normalized peak location and height (k_p, Z_p) of the spectrum $E_\Omega(k)$ in Fig. 3(b); (a) k_p vs R_λ and (b) Z_p vs R_λ.

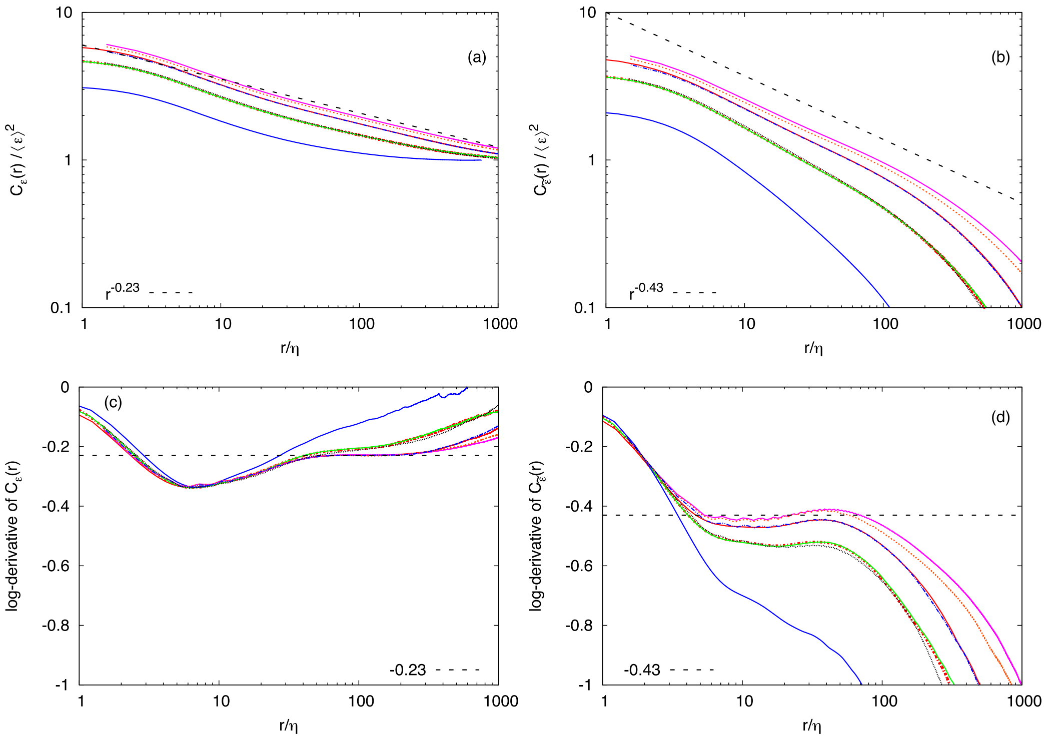

FIG. 7. Correlations (a) $C_\epsilon(r)$ and (b) $C_{\tilde{\epsilon}}(r)$ vs r/η normalized by $\langle\epsilon\rangle^2$; (c) the logarithmic derivatives of $C_\epsilon(r)$ and (d) $C_{\tilde{\epsilon}}(r)$ vs r/η. The colored lines have the same meaning as in Fig. 3.

spectrum $E_{\tilde{\epsilon}}(k)$ obtained in the previous subsection. The correlation $C_\epsilon(r)$ was then computed using (15), based on the $C_{\tilde{\epsilon}}(r)$ thus obtained. Figures 7(c) and 7(d) present the logarithmic derivatives $\xi_{C_\epsilon,r}(r)$ and $\xi_{C_{\tilde{\epsilon}},r}(r)$, respectively, also plotted against r/η. Here $\xi_{\Phi,r}(r)$ is defined by (24) with $\Phi = C_\epsilon(r)$ or $C_{\tilde{\epsilon}}(r)$. Figure 8 displays the same quantities as in Fig. 7 but plotted against r/L instead of r/η.

As seen in Figs. 7 and 8, the high-R_λ DNS data show that $C_\epsilon(r)$ locally follows a power-law behavior of the form

$$C_\epsilon(r) \propto r^{-\mu_{C\epsilon}}, \quad (\mu_{C\epsilon} \approx 0.23), \tag{29}$$

within a range, denoted as $I_{C\epsilon}$, that is around $r/\eta \approx 100$ or $r/L \approx 0.03$, in which $C_{\tilde{\epsilon}}(r)/\langle\epsilon\rangle^2 \sim 1$ [see Figs. 7(a) and 7(c) and Figs. 8(a) and 8(c)]; here the symbol "$\sim$" denotes the equality in the order of magnitude. Similarly, $C_{\tilde{\epsilon}}(r)$ fits well to a local power-law form,

$$C_{\tilde{\epsilon}}(r) \propto r^{-\mu_{C\tilde{\epsilon}}}, \quad (\mu_{C\tilde{\epsilon}} \approx 0.43), \tag{30}$$

in a range, denoted as $I_{C\tilde{\epsilon}}$, which corresponds approximately to $r/\eta \approx 40$ or $r/L \approx 0.01$ [see Figs. 7(b) and 7(d) and Figs. 8(b) and 8(d)]. The ranges $I_{C\epsilon}$ and $I_{C\tilde{\epsilon}}$ are not exactly the same, but they are relatively close to each other.

The arrows in Fig. 8(b) indicate three different Reynolds-number cases at $k_{\max}\eta = 4$. It is observed that the range of scales for which $C_{\tilde{\epsilon}}(r)/\langle\epsilon\rangle^2 > 1$ expands with increasing Reynolds number; to guide the eye, one horizontal and one vertical dotted line are shown to indicate the r/L value at which $C_{\tilde{\epsilon}}(r)/\langle\epsilon\rangle^2 \approx 1$, labeled as r_C/L in the figure.

Figures 9 and 10 present the same types of plots as Figs. 7 and 8, respectively, but for the case $f = \Omega$. Similar observations to those made for $C_\epsilon(r)$ and $C_{\tilde{\epsilon}}(r)$ can also be drawn from Figs. 9

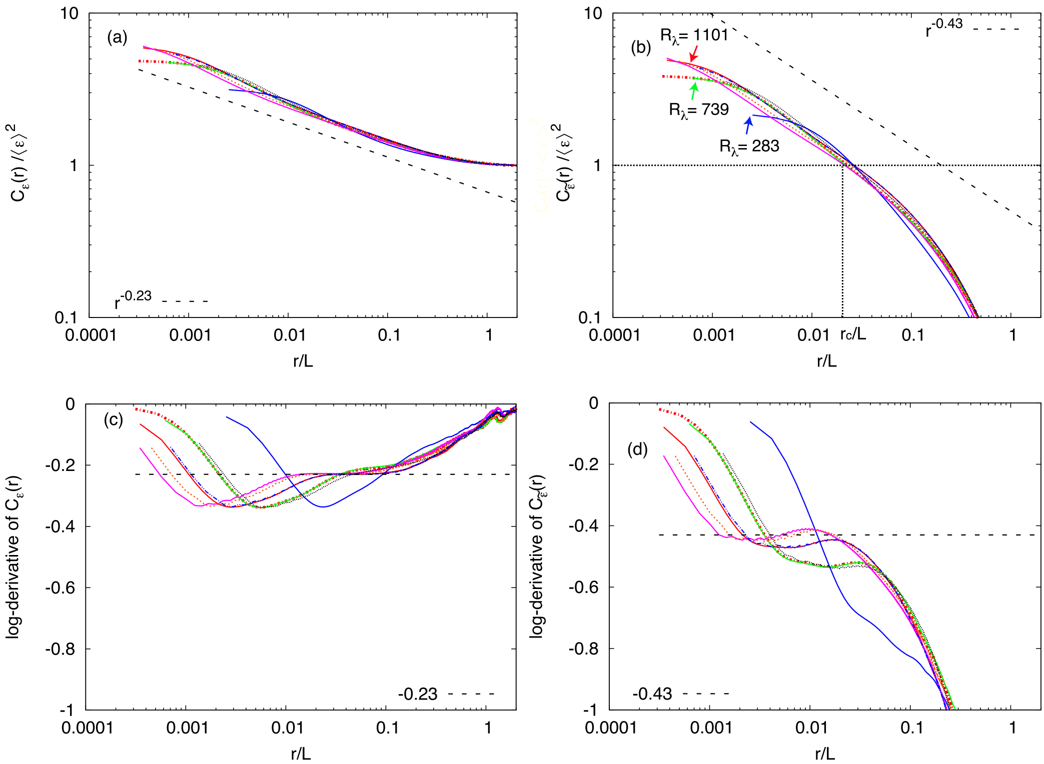

FIG. 8. The same as Fig. 7 but vs r/L.

and 10 regarding $C_\Omega(r)$ and $C_{\tilde{\Omega}}(r)$. As seen in Figs. 9 and 10, the high-R_λ DNS data show that $C_\Omega(r)$ follows a local power-law behavior:

$$C_\Omega(r) \propto r^{-\mu_{C\Omega}}, \quad (\mu_{C\Omega} \approx 0.23), \tag{31}$$

within a range, denoted as $I_{C\Omega}$, that is around $r/\eta \approx 100$ or $r/L \approx 0.03$, where $C_{\tilde{\Omega}}(r)/\langle\Omega\rangle^2 \sim 1$ [see Figs. 9(a) and 9(c) and Figs. 10(a) and 10(c)]. Similarly, $C_{\tilde{\Omega}}(r)$ exhibits a local power-law behavior:

$$C_{\tilde{\Omega}}(r) \propto r^{-\mu_{C\tilde{\Omega}}}, \quad (\mu_{C\tilde{\Omega}} \approx 0.43), \tag{32}$$

in a range, denoted as $I_{C\tilde{\Omega}}$, located around $r/\eta \approx 40$ or $r/L \approx 0.01$ [see Figs. 9(b), 9(d) and 10(b), 10(d)]. The ranges $I_{C\Omega}$ and $I_{C\tilde{\Omega}}$ are not exactly the same, but they are relatively close to each other. The statistical quantities considered in this subsection, together with the corresponding scaling exponents and the scale ranges used to evaluate them, are summarized in Table II.

It can be seen in panels (b) and (d) of Figs. 7–10 that both $C_{\tilde{\varepsilon}}(r)$ and $C_{\tilde{\Omega}}(r)$ decrease monotonically with increasing r. Figure 10(b) shows that the range of scales for which $C_{\tilde{\Omega}}(r)/\langle\Omega\rangle^2 > 1$

TABLE II. Scaling exponents of correlation functions in physical space and the characteristic scale ranges used to evaluate the scaling exponents.

Quantity	Component	Scaling exponent	Scaling range
$C_\varepsilon(r)$	Total	$\mu_{C\varepsilon} \approx 0.23$	Around $r \approx 100\eta$ (or $\approx 0.03L$)
$C_\Omega(r)$	Total	$\mu_{C\Omega} \approx 0.23$	Around $r \approx 100\eta$ (or $\approx 0.03L$)
$C_{\tilde{\varepsilon}}(r)$	Fluctuation	$\mu_{C\tilde{\varepsilon}} \approx 0.43$	Around $r \approx 40\eta$ (or $\approx 0.01L$)
$C_{\tilde{\Omega}}(r)$	Fluctuation	$\mu_{C\tilde{\Omega}} \approx 0.43$	Around $r \approx 40\eta$ (or $\approx 0.01L$)

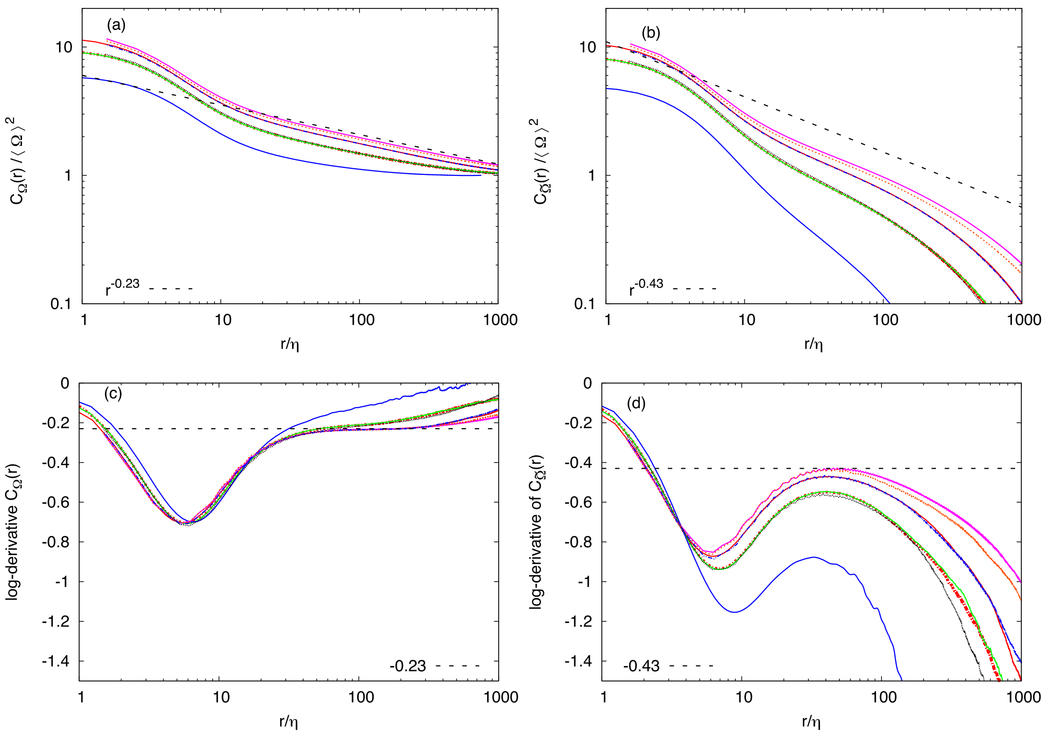

FIG. 9. The same as Fig. 7 but for correlations $C_\Omega(r)$ and $C_{\tilde{\Omega}}(r)$.

expands with increasing Reynolds number, consistent with the corresponding behavior for the energy dissipation rate. Both $C_{\tilde{\epsilon}}(r)$ and $C_{\tilde{\Omega}}(r)$ become comparable in magnitude to $\langle\epsilon\rangle^2$ and $\langle\Omega\rangle^2$, respectively, at a certain scale, denoted here as r_C. According to the present high-R_λ DNS results, this scale is approximately given by $r_C/\eta \approx 100$ and $r_C/L \approx 0.02$. It should be noted that these estimates are based on DNSs with $R_\lambda < 1740$. They do not exclude the possibility that r_C/η and/or r_C/L may vary with R_λ (e.g., see Fig. 5 of Praskovsky and Oncley [14] for the variation of r_C/η). These estimates also do not rule out the possibility that r_C/η and/or r_C/L are nonuniversal in the sense that they may depend on boundary conditions and/or forcing mechanisms.

E. Second-order moments of local averages

Let $\phi_r(\mathbf{x})$ be the local average defined by (2) but with ϵ replaced by a general scalar field ϕ. Then we have

$$\langle {\phi_r}^2 \rangle = \frac{1}{V_r^2} \int_{|\mathbf{h}|<r} d\mathbf{h} \int_{|\mathbf{h}'|<r} d\mathbf{h}' C_\phi(\mathbf{x}+\mathbf{h}, \mathbf{x}+\mathbf{h}'), \tag{33}$$

where $C_\phi(\mathbf{y}, \mathbf{y}') \equiv \langle \phi(\mathbf{y})\phi(\mathbf{y}')\rangle$ is the two-point correlation function.

When the field is statistically homogeneous, a standard manipulation (see the Appendix) gives the following exact formula:

$$\langle {\phi_r}^2 \rangle = 9 \int_0^\infty dk\, E_\phi(k) \frac{[\sin(kr) - kr\cos(kr)]^2}{(kr)^6}. \tag{34}$$

Equation (34) shows that once the spectrum $E_\phi(k)$ is known, the quantity $\langle {\phi_r}^2 \rangle$ can be computed directly—without explicitly generating or filtering the field via $\widehat{\phi_r}(\mathbf{k})$ or evaluating the spatial average $\phi_r(\mathbf{x})$ as defined by (2).

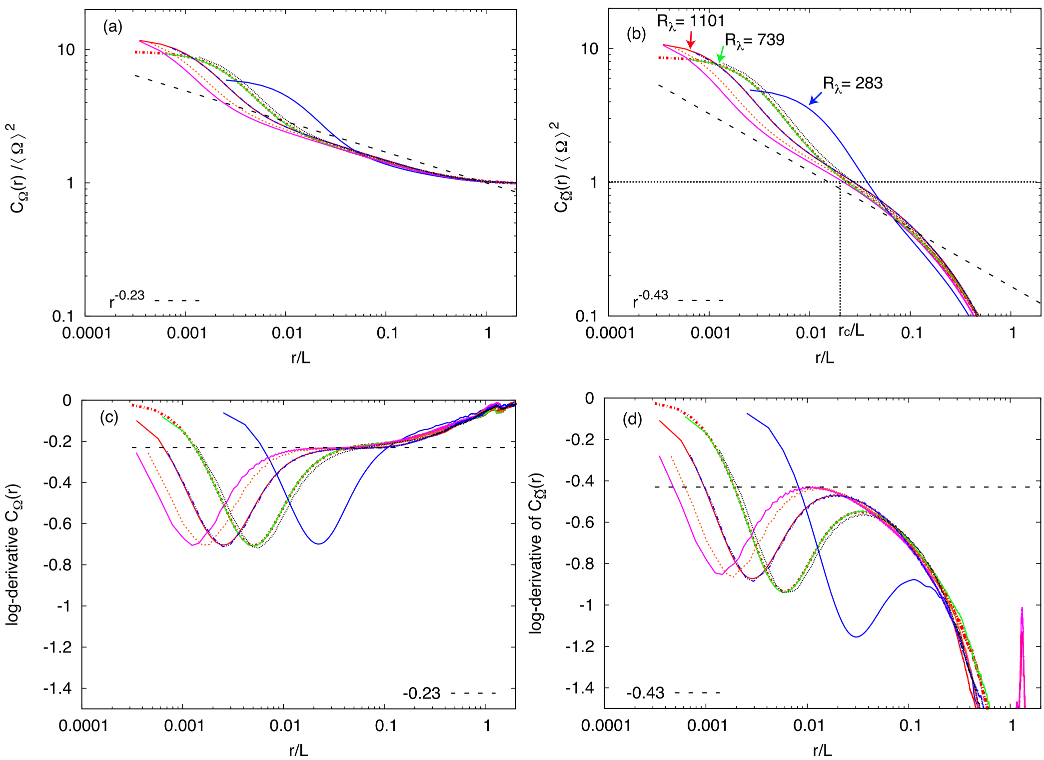

FIG. 10. The same as Fig. 9 but vs r/L.

Figures 11(a) and 11(b) show the second-order moments $\langle \epsilon_r{}^2\rangle$ and $\langle \widetilde{\epsilon}_r{}^2\rangle$, respectively, plotted against r/η. These moments were computed using (34) and the spectrum $E_\epsilon(k)$ discussed in Sec. II C. Figures 11(c) and 11(d) present the corresponding logarithmic derivatives, $\xi_{\langle\epsilon_r{}^2\rangle,r}(r)$ and $\xi_{\langle\widetilde{\epsilon}_r{}^2\rangle,r}(r)$, also plotted versus r/η. Figure 12 displays the same quantities as Fig. 11 but plotted as functions of r/L instead of r/η.

As seen in Figs. 11 and 12, the high-R_λ DNS results show that $\langle \epsilon_r{}^2\rangle$ follows a local power-law behavior:

$$\left\langle \epsilon_r{}^2\right\rangle \propto r^{-\mu_\epsilon}, \quad (\mu_\epsilon \approx 0.23), \tag{35}$$

within a range of r/η, denoted as I_ϵ, that is around $r/\eta \approx 100$ or $r/L \approx 0.03$, where $\langle \epsilon_r{}^2\rangle / \langle\epsilon\rangle^2 \sim 1$ [see Figs. 11(a), 11(c), and 12(a), 12(c)]. Similarly, $\langle \widetilde{\epsilon}_r{}^2\rangle$ exhibits a local power-law scaling:

$$\left\langle \widetilde{\epsilon}_r{}^2\right\rangle \propto r^{-\mu_{\tilde\epsilon}}, \quad (\mu_{\tilde\epsilon} \approx 0.43), \tag{36}$$

in a range of r/η, denoted as $I_{\tilde\epsilon}$, centered approximately around $r/\eta \approx 50$ or $r/L \approx 0.01$ [see Figs. 11(b), 11(d) and 12(b), 12(d)]. The ranges I_ϵ and $I_{\tilde\epsilon}$ are not exactly the same, but they are relatively close to each other.

A similar trend is also observed in Figs. 13 and 14, which show the same plots as Figs. 11 and 12 but for $f = \Omega$. It is seen that $\langle \Omega_r{}^2\rangle$ fits well to a power-law form,

$$\left\langle \Omega_r{}^2\right\rangle \propto r^{-\mu_\Omega}, \quad (\mu_\Omega \approx 0.23) \tag{37}$$

in a range of r/η, denoted as I_Ω, that is around $r/\eta \approx 100$ or $r/L \approx 0.03$ [see Figs. 13(a) and 13(c) and 14(a) and 14(c)], while $\langle \widetilde{\Omega}_r{}^2\rangle$ fits well locally to a power-law form

$$\left\langle \widetilde{\Omega}_r{}^2\right\rangle \propto r^{-\mu_{\tilde\Omega}}, \quad (\mu_{\tilde\Omega} \approx 0.43) \tag{38}$$

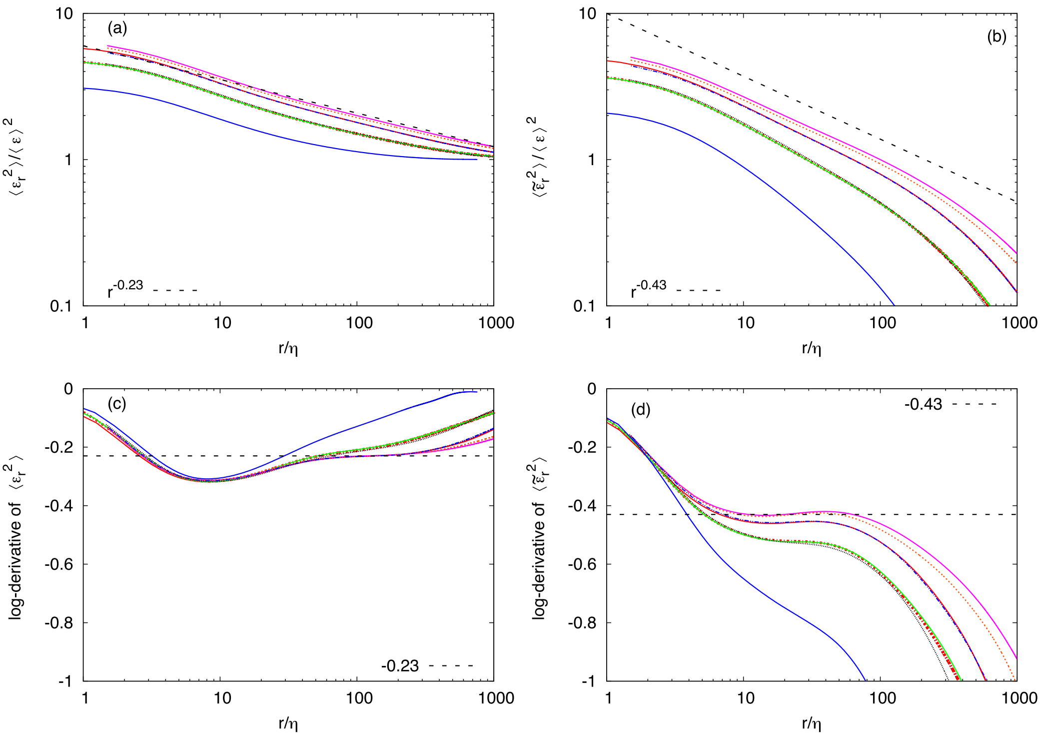

FIG. 11. Local averages (a) $\langle \epsilon_r{}^2 \rangle$ and (b) $\langle \widetilde{\epsilon_r}^2 \rangle$ normalized by $\langle \epsilon \rangle^2$ vs r/η; (c) the logarithmic derivatives of $\langle \epsilon_r{}^2 \rangle$ and (d) $\langle \widetilde{\epsilon_r}^2 \rangle$. The colored lines have the same meaning as in Fig. 3.

in a range of r/η, denoted as $I_{\tilde{\Omega}}$, that is around $r/\eta \approx 50$ or $r/L \approx 0.01$ [see Figs. 13(b) and 13(d) and Figs. 14(b) and 14(d)]. The two ranges I_Ω and $I_{\tilde{\Omega}}$ are not exactly the same but not very far from each other. The scaling exponents and characteristic scale ranges of the local-average statistics are summarized in Table III.

Figures 11(a) and 11(c) appear consistent with Fig. 8 in Yeung and Ravikumar [18] and Fig. 1(a) in Buaria and Sreenivasan [19], respectively. These earlier results were obtained from DNS at R_λ in the range 390–1300 (Yeung and Ravikumar) and at $R_\lambda = 1300$ (Buaria and Sreenivasan). The estimate $\mu_\epsilon \approx 0.23$ in (35), as well as the corresponding estimate $\mu_\Omega \approx 0.23$ in (37), are consistent with the values reported in those studies.

The present estimates of $\mu_{\tilde{\epsilon}} \approx 0.43$ and $\mu_{\tilde{\Omega}} \approx 0.43$ [see (36) and (38)] are also consistent with the results by Buaria and Sreenivasan [19]. Note that, in Fig. 1(b) of their paper [19], what is plotted is the standard deviation, not the variance as stated incorrectly in the caption. This clarification is based on a personal communication with K. R. Sreenivasan. If Fig. 1(b) actually shows standard

TABLE III. Scaling exponents of spherically averaged quantities in physical space and the characteristic scale ranges used to evaluate the scaling exponents.

Quantity	Component	Scaling exponent	Scaling range
$\langle \varepsilon_r^2 \rangle$	Total	$\mu_\varepsilon \approx 0.23$	Around $r \approx 100\eta$ (or $\approx 0.03L$)
$\langle \Omega_r^2 \rangle$	Total	$\mu_\Omega \approx 0.23$	Around $r \approx 100\eta$ (or $\approx 0.03L$)
$\langle \tilde{\varepsilon}_r^2 \rangle$	Fluctuation	$\mu_{\tilde{\varepsilon}} \approx 0.43$	Around $r \approx 50\eta$ (or $\approx 0.01L$)
$\langle \tilde{\Omega}_r^2 \rangle$	Fluctuation	$\mu_{\tilde{\Omega}} \approx 0.43$	Around $r \approx 50\eta$ (or $\approx 0.01L$)

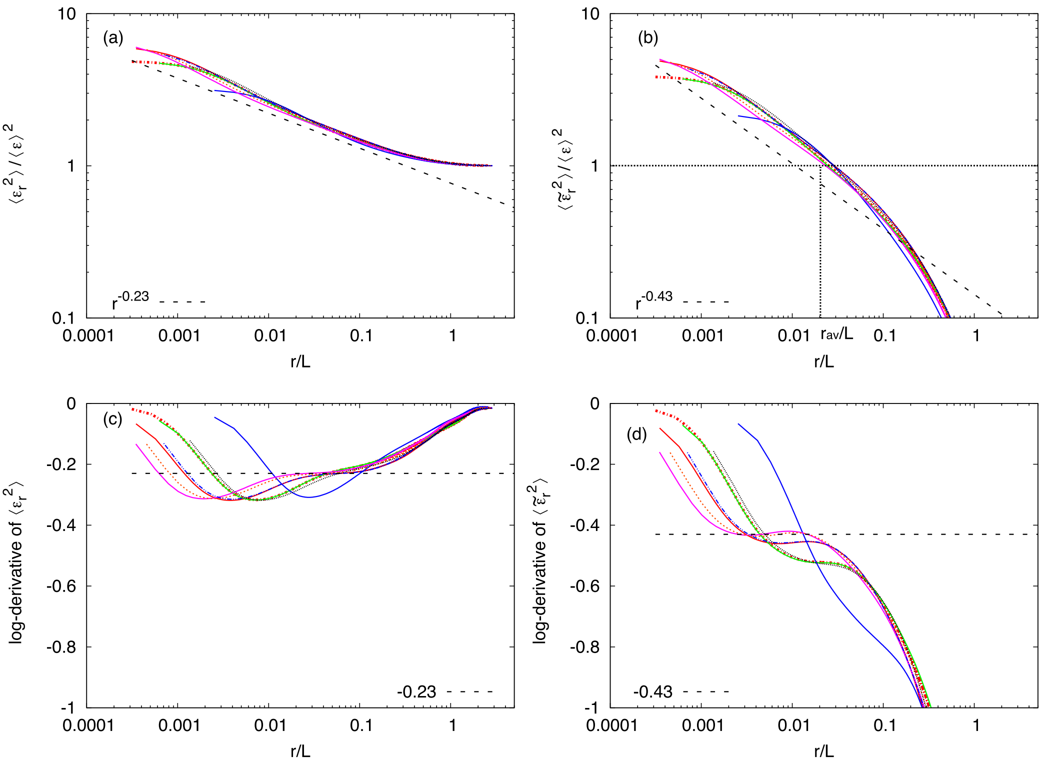

FIG. 12. The same as Fig. 11 but vs r/L.

deviations, then the exponent -0.23 should be interpreted as that of the standard deviation, say, $-\mu_{sd}$, rather than that of the variance, $-\mu_v$. In that case, $\mu_{sd} \approx 0.23$ would imply $\mu_v = 2\mu_{sd} \approx 0.46$, which aligns reasonably well with the present estimates.

It can be seen in panels (b) and (d) of Figs. 11–14 that both $\langle \widetilde{\epsilon}_r{}^2 \rangle$ and $\langle \widetilde{\Omega}_r{}^2 \rangle$ decrease monotonically with increasing r and that they become comparable in magnitude to $\langle \epsilon \rangle^2$ and $\langle \Omega \rangle^2$, respectively, near a certain scale, denoted here as r_{av}. According to the figures, this scale is approximately given by $r_{av}/\eta \approx 100$ and $r_{av}/L \approx 0.02$ in the present high-R_λ DNSs. As in the case of the scale r_C discussed in the previous subsection, these estimates are based on DNSs with $R_\lambda \leqslant 1740$, and they do not exclude the possibility that r_{av}/η and/or r_{av}/L may vary with R_λ. These estimates also do not rule out the possibility that r_{av}/η and/or r_{av}/L are nonuniversal, in the sense that they may depend on boundary conditions and/or forcing mechanisms.

1. Ratios of logarithmic derivatives of correlation functions and local averages

A comparison of Figs. 11(b) and 12(b) shows that, in the high-R_λ DNSs, the curves for different R_λ collapse somewhat more closely when plotted against r/L rather than r/η at larger r (say, $r/\eta \gtrsim 50$ or $r/L \gtrsim 0.01$). A similar tendency is observed for the other quantities shown in (b) of Figs. 7–10, 13, and 14. This behavior contrasts with that of the ratios of logarithmic derivatives discussed below.

Buaria and Sreenivasan [19] plotted the ratio of the logarithmic derivatives of $\langle \Omega_r{}^2 \rangle$ and $\langle \epsilon_r{}^2 \rangle$ (their Fig. 2), and noted that the ratio remains consistently above unity within the inertial subrange. A weak but clear trend toward unity with increasing R_λ was also reported, although the convergence is slow. Figure 15(a) in the present work is consistent with these observations. Figure 15(b) shows the corresponding ratio for the logarithmic derivatives of $C_\Omega(r)$ and $C_\epsilon(r)$. Owing to noisy r dependence at large r/η in the run with $R_\lambda \approx 283$, the corresponding curve is omitted from

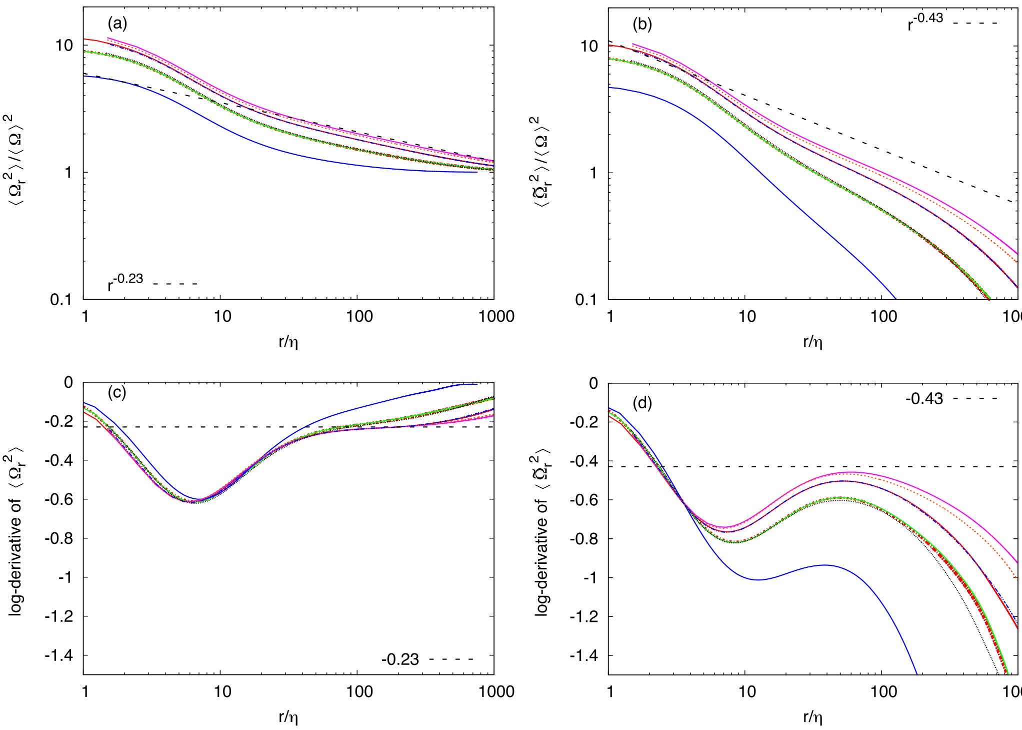

FIG. 13. The same as Fig. 11 but for $\langle \Omega_r{}^2 \rangle$ and $\langle \widetilde{\Omega_r}{}^2 \rangle$.

Fig. 15(b). Trends similar to those seen in Fig. 15(a) are also evident in Fig. 15(b) and likewise appear in the ratios of the logarithmic derivatives of the correlation functions and local averages of the fluctuating components of these quantities (figures omitted).

The ratios of the logarithmic derivatives are more closely aligned at large r when plotted as functions of r/η rather than r/L (figures omitted). At first glance, this may seem puzzling, given that both the local averages and the correlations themselves collapse better with r/L than with r/η, as discussed above. However, this is not surprising in view of the following. First, Fig. 1 shows that the spectra $E_\epsilon(k)$ and $E_\Omega(k)$ are similar at low wave numbers (the L-range) but deviate more significantly at higher wave numbers (the M-range). Second, differentiation with respect to r enhances the contribution of higher wave numbers, implying that the logarithmic derivative is more sensitive to small-scale statistics than the original quantity. These observations suggest that the differences between the logarithmic derivatives are primarily governed by dissipation-range statistics rather than inertial-range statistics.

III. DIFFERENCES BETWEEN EXPONENTS

A. Difference of exponent $\mu_{k\tilde{f}}$ from $\mu_{C\tilde{f}}$ and $\mu_{\tilde{f}}$

According to Eqs. (25), (30), and (36), as well as (26), (32), and (38), the spectral exponent $\mu_{k\tilde{f}}$ (approximately 1/3) differs from the corresponding real-space exponents $\mu_{C_{\tilde{f}}}$ and $\mu_{\tilde{f}}$ (both approximately 0.43) for both $f = \epsilon$ and $f = \Omega$.

At first glance, this appears to contradict the naïve conjecture that, for a given f, the exponents satisfy $\mu_{k\tilde{f}} = \mu_{C\tilde{f}} = \mu_{\tilde{f}}$. This conjecture can be derived from simple power counting or dimensional analysis. Indeed, if the power-law form $E_\phi(k) \propto k^{\mu_{k\tilde{f}}-1}$ (with $\mu_{k\tilde{f}} \approx 1/3$) is substituted into the integrals in Eqs. (28) and (34), then both integrals converge at both the low and

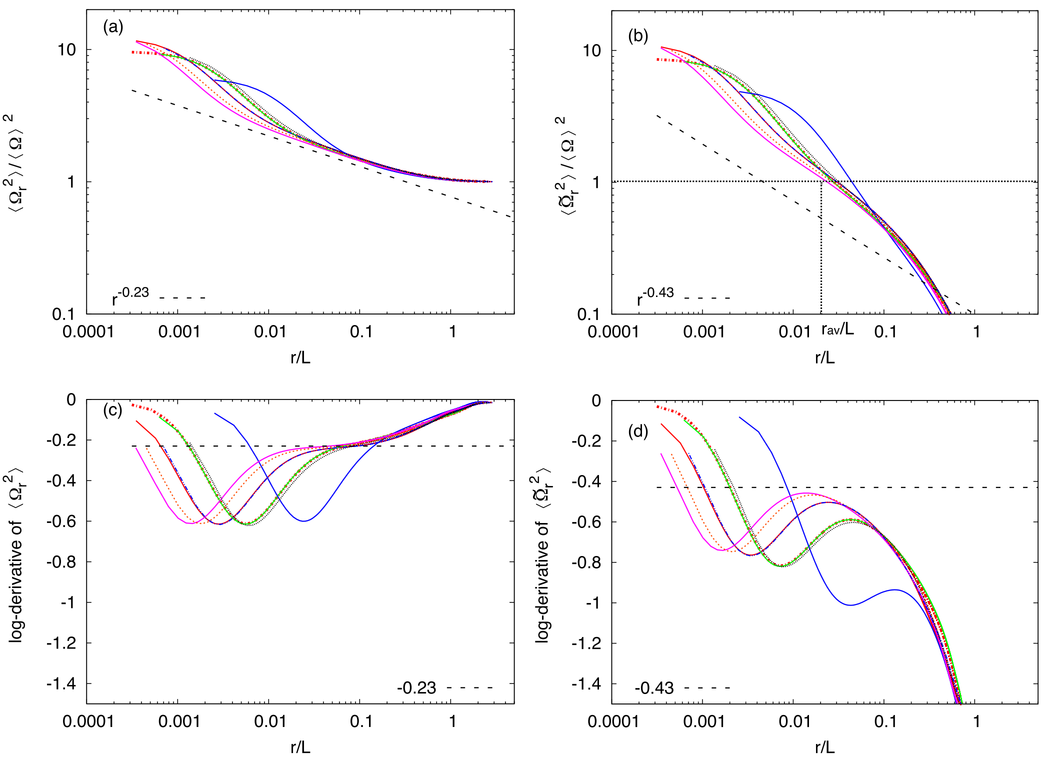

FIG. 14. The same as Fig. 13 but vs r/L.

high-wave-number limits. This suggests that, assuming a sufficiently wide scaling range and negligible contributions from outside it, one would expect $\mu_{k\tilde{f}} = \mu_{C\tilde{f}} = \mu_{\tilde{f}}$ for $\tilde{f} = \tilde{\epsilon}$ and $\tilde{\Omega}$. However, as seen in Fig. 4, the scaling ranges of $E_\phi(k)$ in the present DNSs span at most about one decade in wave number. Therefore, the observed discrepancy between $\mu_{k\tilde{f}}$ and the real-space exponents is not surprising and can be attributed, at least partly, to the limited extent of the inertial subrange. For related discussions of comparisons among spectral and real-space scaling exponents in the context of one-dimensional spectra and surrogate measurements of ϵ, readers may also refer to Praskovsky and Oncley [14] and references cited therein.

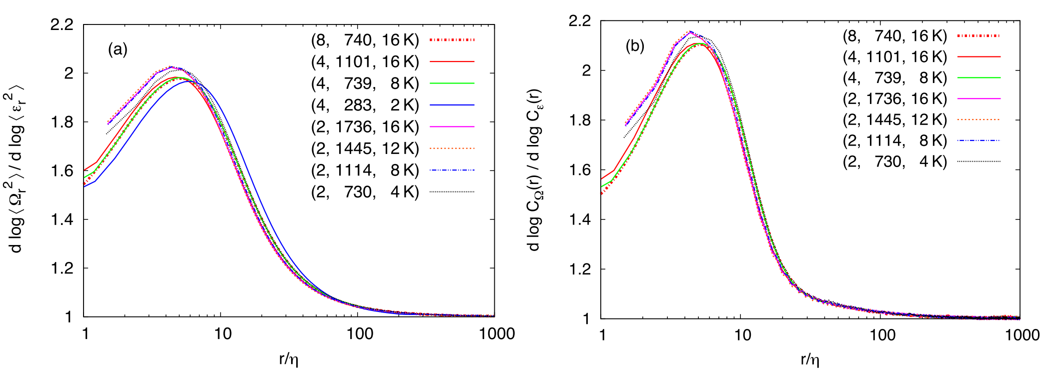

FIG. 15. Ratio of the logarithmic derivatives of (a) $\langle {\Omega_r}^2 \rangle$ and $\langle {\epsilon_r}^2 \rangle$; (b) $C_\Omega(r)$ and $C_\epsilon(r)$.

B. Difference between (μ_{Cf}, μ_f) and $(\mu_{C\tilde{f}}, \mu_{\tilde{f}})$

According to Eqs. (29) and (30), as well as (31) and (32), the exponents $\mu_{C\tilde{f}} \approx 0.43$ are found to be significantly larger than $\mu_{Cf} \approx 0.23$ for both $f = \epsilon$ and $f = \Omega$. Similarly, from Eqs. (35)–(38), we obtain $\mu_{\tilde{f}} \approx 0.43$, again exceeding $\mu_f \approx 0.23$ for both cases. At first glance, these discrepancies appear to contradict the intuitive expectation that $\mu_{Cf} = \mu_{C\tilde{f}}$ and $\mu_f = \mu_{\tilde{f}}$. In what follows, we present a three-step explanation of the origin of these discrepancies, based on steps (i), (ii), and (iii). Then, item (iv) discusses a possible influence of the finite simulation time on the DNS results.

(i) Exact relation and its implications

First, note that

$$F(r) = 1 + \tilde{F}(r), \tag{39}$$

where $F(r) \equiv \Phi(r)/\langle f\rangle^2$ and $\tilde{F}(r) \equiv \tilde{\Phi}(r)/\langle f\rangle^2$, with $(\Phi(r), \tilde{\Phi}(r))$ representing either the pair $(C_f(r), C_{\tilde{f}}(r))$ of two-point correlation functions or the pair $(\langle {f_r}^2\rangle, \langle \widetilde{f_r}^2\rangle)$ of second-order local averages. This identity is verified by (14) and (17).

If $\tilde{\Phi}(r)$ follows a power law with a constant exponent over some range of r, and if $\tilde{F}(r) \gg 1$ holds throughout that range, then it would be reasonable to approximate $F(r) \approx \tilde{F}(r)$, thereby justifying the naïve conjecture that $\Phi(r)$ and $\tilde{\Phi}(r)$ share the same scaling exponent. However, as shown in panel (b) of Figs. 7–14, the condition $\tilde{F}(r) \gg 1$ is not satisfied in the scale ranges where the exponents are estimated. Therefore, the observed differences between the exponents of $\Phi(r)$ and $\tilde{\Phi}(r)$ are not unexpected in light of (39). A constraint equivalent to (39) for the two-point correlations $C_\epsilon(r)$ and $C_{\tilde{\epsilon}}(r)$ has also been emphasized in studies of energy dissipation statistics by Praskovsky and Oncley [14,28], who highlighted its significance in considering their scaling behavior.

The first terms on the right-hand sides of (14) and (17) represent contributions from the mean component $\langle f\rangle$, while the second terms account for the contributions from the fluctuating part $\tilde{f}$. As indicated by panels (b) in Figs. 7–14, the normalized fluctuating contribution $\tilde{F}(r)$ becomes approximately unity at a certain characteristic scale, denoted r_*. Based on these observations—particularly in the high-R_λ regime—it appears that in high-Re turbulence, at least three distinct scale ranges can be identified:

(1) W-range (weak-fluctuation range): $r \gg r_*$, where $0 < \tilde{F} \ll 1$,
(2) T-range (transitional range): $r \sim r_*$, where $\tilde{F} \sim 1$, and
(3) S-range (strong-fluctuation range): $r_* \gg r \gg \eta$, where $\tilde{F} \gg 1$.

Here the characteristic scale r_* may correspond to either the correlation scale r_C or the averaging scale $r_{\rm av}$. In the present DNS results, where R_λ reaches up to approximately 1740, this characteristic scale is found to be around $r_* \approx 0.02L$. (Note that the possibility that r_*/L depends on R_λ and/or is not universal cannot be ruled out.)

In the W- and S-ranges, $\Phi(r)$ is respectively dominated by the mean (independent of r) and fluctuating contributions, while the T-range represents an intermediate regime where both are comparable. Accordingly, the local scaling exponents extracted from different ranges need not coincide, reflecting the scale-dependent relative contributions of the mean and fluctuating components implied by (39).

(ii) Condition for the existence of the inertial subrange satisfying $\tilde{F}(r) \gg 1$

It is natural to assume that in the S-range of turbulence at sufficiently high R_λ, both $\tilde{\Phi}(r)$ and $\Phi(r)$ may be well approximated by power-law forms with the same exponent, denoted by $\mu_{\Phi,S}$. However, it is not guaranteed that $\mu_{\Phi,S}$ is close to the present DNS-based values of $\mu_f(\approx 0.23)$ or $\mu_{\tilde{f}}(\approx 0.43)$, since these exponents were estimated from data in the T-range—not the S-range—based on DNS results at $R_\lambda \leqslant 1740$. To assess the relevance of intermittency exponents observed in measurements or DNS as candidates for $\mu_{\Phi,S}$ in the S-range at asymptotically high Reynolds numbers, it is desirable not only to ensure that R_λ is sufficiently large but also to verify that the condition $\tilde{F}(r) \gg 1$ holds throughout the scale range being analyzed.

As discussed above, our DNS results suggest that the condition $\tilde{F}(r) \gg 1$ is unlikely to be satisfied unless

$$r \ll r_*, \quad \text{where} \quad r_* \approx \frac{1}{D_L} L, \tag{40}$$

in which $D_L \approx 100/2$, under the conditions of our DNS. If one is interested in the "inertial subrange" scaling, then the relevant range must also satisfy

$$r \gg D_\eta \eta, \tag{41}$$

where D_η is a constant typically of order 10 or greater. To simultaneously satisfy both conditions—i.e., to observe an inertial subrange in which $\tilde{F}(r) \gg 1$ holds—the range of scales r must lie within

$$D_\eta \eta \ll r \ll r_* \approx \frac{1}{D_L} L. \tag{42}$$

This leads to the constraint

$$\frac{L}{\eta} \ggg\gg D_L D_\eta. \tag{43}$$

Assuming, for example, $D_\eta \approx 50$ and $D_L \approx 100/2$, we obtain $D_L D_\eta \approx 2500$. As shown in Table I, the largest value of L/η achieved in our DNSs with $k_{\max}\eta \geqslant 2$ is from Run 16384-2 ($R_\lambda \approx 1736$), where $L/\eta \approx 1.10/(2.56 \times 10^{-4}) \approx 4300$. This implies that in our DNSs, which reach R_λ up to 1736, the existence of an inertial subrange satisfying the strong inequalities in (42) is questionable.

(iii) Interpretation of the relationship between exponents

Finally, to gain quantitative insight into the relationship between the exponents 0.23 and 0.43, consider the identity (39), which leads to

$$\xi_{F,r}(r) \equiv \frac{d \log F(r)}{d \log r} = \frac{r}{F} \cdot \frac{d\tilde{F}}{dr} = \frac{r}{1+\tilde{F}} \cdot \frac{d\tilde{F}}{dr}. \tag{44}$$

According to Figs. 7–14, $\tilde{F}(r)$ can be locally approximated near $r \approx r_*$ by a power law of the form $\tilde{F}(r) \approx \gamma r^{-\beta}$, with $\beta \approx \mu_*$, where γ is a constant and μ_* denotes either $\mu_{C\tilde{f}}$ or $\mu_{\tilde{f}}$ (both approximately 0.43). This gives

$$r\frac{d\tilde{F}}{dr} \approx -\gamma\beta r^{-\beta} \approx -\beta\tilde{F}, \tag{45}$$

so that at $r \approx r_*$, where $\tilde{F}(r) \approx 1$ and $\beta \approx \mu_*$, we obtain

$$\xi_{F,r}(r) \approx -\tfrac{1}{2}\mu_* \approx -\tfrac{0.43}{2}. \tag{46}$$

This result illustrates that near the transition scale $r \approx r_*$, where the fluctuation contribution becomes comparable to the mean, the local scaling behavior of $F(r)$ is governed by an effective exponent approximately $-\mu_*/2$. This provides a natural explanation for the observed discrepancy between the exponents $\mu_f \approx 0.23$ and $\mu_{\tilde{f}} \approx 0.43$ in terms of the scale-dependent influence of fluctuation intensity.

This is consistent with Figs. 7–14, which show that $\xi_{F,r}(r)$ is not far from -0.23 at $r \approx r_*$, where $r_*/\eta \approx 100$. Equation (39) and the estimate (46) indicate that even if $\xi_{F,r}(r) \approx -\mu_*/2$ at $r \sim r_*$, this does not imply that $\Phi(r)$ obeys a global power-law scaling of the form $\Phi(r) \propto r^{-\mu_*/2}$. Such an approximation is only valid locally around $r \sim r_*$ and should not be extrapolated beyond that range.

The present DNS-based estimates of 0.23 (or 0.43/2) and 0.43 are consistent with previously reported intermittency exponents for the correlations and local averages of the total dissipation rate ϵ and its fluctuating component $\tilde{\epsilon}$, respectively. In particular, these estimates are in agreement with the values reported by Anselmet *et al.* [12], who found an intermittency exponent of approximately 0.2 ± 0.05 for ϵ, and a value close to 0.5 for $\tilde{\epsilon}$, based on laboratory experiments at R_λ up to 892. Likewise, the present estimates of 0.23 and 0.43 for ϵ and $\tilde{\epsilon}$, respectively, are consistent with those reported by Praskovsky and Oncley [14,28], who analyzed both laboratory experiments and atmospheric observations at much higher Reynolds numbers, up to $R_\lambda \approx 12{,}700$.

(iv) Effect of the finite simulation time

As seen in Table I, the simulation time t_F in our high-R_λ DNS runs is not very large as compared to the large-eddy turnover time T. Although the potential influence of this relatively short simulation time remains an issue to be clarified in general and may deserve further investigation, such an analysis is not readily feasible at present. Nevertheless, the following observations suggest that its influence on the estimated intermittency exponents is unlikely to be substantial:

(i) the reasonable agreement between the present estimates of intermittency exponents and those obtained from earlier laboratory experiments [12] and from both laboratory experiments and atmospheric observations [14,28], as noted above;

(ii) the consistency between the present estimates of the exponents μ_ϵ and μ_Ω and those reported in other DNS studies [18,19] (see Sec. II D); and

(iii) the consistency of the exponents obtained from different runs of our high-R_λ DNSs, despite differences in run conditions, such as initial conditions that differ at least to the extent that can be inferred from Table I and the values of R_λ.

It may be worth noting, however, that the DNS-based estimate of 0.43 for the correlation $C_{\tilde\epsilon}(r)$ differs somewhat from the value of 0.27 reported by Sreenivasan and Kailasnath [13], based on atmospheric data with R_λ ranging from 1500 to 2000, although the DNS-based estimate of 0.23 for $C_\epsilon(r)$ is not far from their reported value of 0.25. According to their Figs. 1 and 3, the difference between $C_\epsilon(r)$ and $C_{\tilde\epsilon}(r)$ appears to be relatively small. In contrast, a substantial, or at least non-negligible, difference is observed in Fig. 12 ($R_\lambda = 536$) of Anselmet *et al.* [12] and in Fig. 5 ($R_\lambda =$ 2000–12 700) of Praskovsky and Oncley [28].

C. Exponents of energy spectrum and second-order structure function

In studies of small-scale intermittency in high-Re turbulence, including K62, it is commonly argued that the second-order longitudinal structure function $S_2^L(r)$ and the energy spectrum $E(k)$ are given by the following intermittency-corrected forms:

$$S_2^L(r) = C_S\langle\epsilon\rangle^{2/3} r^{2/3}(r/L)^{-\mu_S}, \tag{47}$$

in the inertial subrange $L \gg r \gg \eta$, and

$$E(k) = C_E\langle\epsilon\rangle^{2/3} k^{-5/3}(kL)^{-\mu_E}, \tag{48}$$

in the spectral inertial subrange $1/L \ll k \ll 1/\eta$. Here C_S and C_E are constants that may depend on the large-scale structure of the flow, while μ_S and μ_E represent universal intermittency correction exponents to the $r^{2/3}$ and $k^{-5/3}$ scalings predicted by K41.

If the r-range over which $S_2^L(r)$ obeys (47) is sufficiently extended, and μ_S lies within a suitable range, then the corresponding energy spectrum $E(k)$ obeys (48) over the inertial subrange, with $\mu_E = \mu_S$. Conversely, if $E(k)$ exhibits clear scaling behavior as in (48), and μ_E is within an appropriate range, then (47) follows with $\mu_S = \mu_E$. According to the K62 theory, the exponent μ_S is related to the intermittency of the energy dissipation rate through the relation

$$\mu_S = \frac{\mu}{9}, \tag{49}$$

where μ denotes the variance coefficient in the log-normal model for $\log\epsilon$, as defined in (3).

A series of DNSs [20,29] with Taylor-scale Reynolds numbers up to approximately $R_\lambda \approx 2300$ showed the existence of a wave-number range—approximately $5\times10^{-3} < k\eta < 2\times10^{-2}$—in which the energy spectrum $E(k)$ fits well to the intermittency-corrected scaling form in (48) with a positive exponent $\mu_E > 0$. Ishihara *et al.* [20] referred to this region as the tilted range, and the DNS data yielded an estimate of $\mu_E \approx 0.12$. This range lies at wave numbers much smaller than the bump wave number k_b, defined as the characteristic wave number at which $E(k)/k^{5/3}$ exhibits a pronounced local maximum; typically, $k_b\eta \approx 0.1$.

The existence of a similar scaling range with $\mu_E > 0$ at $k \ll k_b$ has also been confirmed in recent large-scale DNSs by Yeung *et al.* [23], which achieved $R_\lambda \approx 2500$ with a resolution of up to $32\,768^3$ grid points. According to Fig. 3(b) of their study, a comparable value of $\mu_E \approx 0.12$ is observed at $k\eta \approx 1 \times 10^{-2}$. The fact that these two groups—employing different numerical schemes, forcing methods, and levels of arithmetic precision—obtained consistent results lends credibility to the robustness of the observed intermittency correction in the tilted range. Moreover, these findings are broadly consistent with earlier spectral data from Donzis and Sreenivasan [30]. Specifically, if one overlays a line with slope -0.12 (corresponding to $\mu_E = 0.12$) on Fig. 1 of their paper, or a horizontal line at $d[\log E(k)]/d[\log k] = -(5/3 + 0.12)$ in Fig. 4(b), then the agreement with the DNS spectra is clear—or at the very least, not inconsistent.

However, the DNS-based estimate $\mu_E \approx 0.12$ appears significantly larger than the value $\mu_E \approx 0.03$ predicted by the K62 relation (49) using $\mu_S = \mu_E$ and $\mu \approx 0.25$—a value widely accepted in the literature for the intermittency parameter (see, for example, Sreenivasan and Kailasnath [13]).

Regarding the second-order longitudinal structure function $S_2^L(r)$, the series of DNSs by Ishihara *et al.* [21] reported a scale range, approximately $100 < r/\eta < 400$, referred to as the tilted range, in which $S_2^L(r)$ fits well to the intermittency-corrected form given in (47), with $\mu_S \approx 0.065$. The existence of such a range with a positive intermittency exponent $\mu_S > 0$ has also been observed in experiments by Küchler *et al.* [31], conducted at Reynolds numbers up to $R_\lambda \approx 5300$. Their measurements of the function $S_2^L(r)$ appear consistent with the DNS results (see their Fig. 1), lending further credibility to the reliability of the DNS results.

The difference between the exponent $\mu_S \approx 0.065$ and the corresponding value $\mu_E \approx 0.12$ for the energy spectrum (discussed earlier) is not surprising, given the limited extent of the inertial scaling ranges. While in principle one expects $\mu_S = \mu_E$ in the limit of a sufficiently broad and well-defined inertial subrange, deviations are expected when the scaling region is narrow.

The value $\mu_S \approx 0.065$ is closer to the K62-based theoretical prediction $\mu_S \approx 0.03$, obtained via (49) with $\mu \approx 0.25$, although still significantly larger. If, instead, one uses $\mu \approx \mu_* \approx 0.43$—the exponent obtained from the scaling of dissipation fluctuations in the present DNSs—then (49) yields $\mu_S = \mu/9 \approx 0.43/9 \approx 0.048$. Although $\mu_S \approx 0.065$ remains larger than 0.048, it is closer to this value than to the classical estimate $0.25/9 \approx 0.03$.

One may naturally question the origin of the discrepancy between the exponents $\mu_E \approx 0.12$ (or $\mu_S \approx 0.065$) obtained from DNSs and the smaller value $\mu_S = \mu/9 \approx 0.03$ predicted by (49) with $\mu \approx 0.25$, which is widely cited in the literature. While the reliability of (49) itself may also be subject to scrutiny, the reason for this discrepancy remains unclear. At the current stage of understanding, identifying the underlying cause appears to be a difficult task and lies beyond the scope of the present paper.

However, regarding the discrepancy between the exponents $\mu_E \approx 0.12$ (or $\mu_S \approx 0.065$) obtained from DNSs and the value of μ_S inferred from (49) with $\mu = \mu_f \approx 0.23$, it is worthwhile to recall the following:

(i) As discussed in Sec. III B, the estimate $\mu_f \approx 0.23$ was derived from data in the T-range of turbulence, based on DNSs at R_λ up to 1740. It remains unclear whether this exponent is representative of the scaling exponent $\mu_{\Phi,S}$ that would characterize the S-range at sufficiently high Reynolds numbers. Note that if we assume $E(k)$ is predominantly influenced by the statistics at scales for which kr is of order unity, then the spectrum $E(k)$ in the tilted range, approximately given by $5 \times 10^{-3} < k\eta < 2{\times}10^{-2}$, is mainly influenced by statistics at scales where r/η is of order 10^2. According to Fig. 11, this r-range lies within the T-range and/or W-range, but not within the S-range, in our high-R_λ DNSs.

(ii) According to a series of DNSs by Ishihara *et al.* [20,21], conducted at R_λ up to approximately 2300, both the energy spectrum $E(k)$ and the structure function $S_2^L(r)$ exhibit good agreement with the intermittency-corrected forms given by Eqs. (48) and (47) within the so-called tilted ranges. However, the coefficients C_E and C_S in these expressions are found to depend systematically on R_λ, exhibiting simple power-law behavior. This implies that $E(k)$ and $S_2^L(r)$ in these ranges are not determined solely by $\langle\epsilon\rangle$, L, and r, but also retain an explicit dependence on R_λ.

To the authors' knowledge, no existing theory—including K62 or related intermittency models—provides an explanation for the observed power-law dependencies of C_E and C_S on R_λ. This raises doubts about the applicability of such theories to the tilted ranges and underscores the need for further theoretical development to account for these dependencies.

The DNSs by Ishihara *et al.* also suggest the possibility that, at scales larger than those associated with the tilted ranges, there exists an additional scaling range in which the intermittency correction exponents for $E(k)$ and $S_2^L(r)$ are significantly smaller—if not vanishing—compared to those observed in the tilted ranges. The coexistence of multiple scaling ranges for $E(k)$ at low wave numbers ($k\eta \ll 1$) in high-Re turbulence has also been indicated by atmospheric measurements by Tsuji [32].

IV. CONCLUSIONS

We have studied the statistical properties of the energy dissipation rate ϵ and enstrophy Ω, based on data from large-scale DNSs with up to $16\,384^3$ grid points, without resorting to surrogate quantities. The DNSs include a simulation with $R_\lambda \approx 1736$ and $k_{\max}\eta \approx 2$, as well as one with $R_\lambda \approx 740$ and $k_{\max}\eta \approx 8$.

The statistics studied include the following :

(i) the spectra $E_\epsilon(k)$ and $E_\Omega(k)$ of the second-order moments of ϵ and Ω, respectively;

(ii) the two-point correlation functions $C_\epsilon(r)$ and $C_\Omega(r)$ of ϵ and Ω, respectively, together with those of their fluctuating components, i.e., $C_{\tilde{\epsilon}}(r)$ and $C_{\tilde{\Omega}}(r)$; and

(iii) the second-order moments $\langle {\epsilon_r}^2\rangle$ and $\langle {\Omega_r}^2\rangle$ of the local averages of ϵ and Ω, together with those of their fluctuating components, i.e., $\langle \widetilde{\epsilon_r}^2\rangle$ and $\langle \widetilde{\Omega_r}^2\rangle$.

In high-Reynolds-number DNSs with $1100 < R_\lambda < 1740$, the spectra $E_\epsilon(k)$ and $E_\Omega(k)$ exhibit local power-law behavior of the form $E_f(k) \propto k^{\mu_{kf}-1}$, where f denotes either ϵ or Ω, and the exponent $\mu_{kf} \approx 1/3$ is observed within a wave-number range around $k\eta \approx 0.02$. The DNS results show that $E_\Omega(k) > E_\epsilon(k)$ in a range near $k\eta \approx 0.1$, while the two spectra become nearly equal in the higher wave-number range, say, for $k\eta \gtrsim 3$. At $k\eta \gtrsim 3$, the spectra from Run 16384-8 ($R_\lambda \approx 740,\ k_{\max}\eta \approx 8$) exhibit a slight concavity, when $\log E_f(k)$ is plotted against k.

The correlation functions and the local averages satisfy the identities

$$C_f(r) = \langle f\rangle^2 + C_{\tilde{f}}(r), \quad \langle {f_r}^2\rangle = \langle f\rangle^2 + \langle \widetilde{f_r}^2\rangle, \tag{50}$$

where $\tilde{f} \equiv f - \langle f\rangle$ and $\langle f\rangle$ is independent of r. This relation reflects the decomposition of the full second-order statistics into contributions from the mean and the fluctuating component of f. According to the DNS results, both the two-point correlation functions $C_\epsilon(r)$ and $C_\Omega(r)$, as well as the second-order moments $\langle {\epsilon_r}^2\rangle$ and $\langle {\Omega_r}^2\rangle$, decrease monotonically with increasing r. There exists a characteristic scale, denoted r_*, at which both the correlation functions $C_{\tilde{f}}(r)$ and the second-order moments $\langle \widetilde{f_r}^2\rangle$ of the fluctuating components become comparable in magnitude to $\langle f\rangle^2$.

The DNS results suggest that, in turbulence at sufficiently high R_λ, there exist at least three distinct scale ranges—referred to as the W-range (weak fluctuations), T-range (transitional), and S-range (strong fluctuations)—characterized as follows:

(i) W-range: $r \gg r_*$, with $\tilde{\Phi}(r) \ll \langle f\rangle^2$,

(ii) T-range: $r \sim r_*$, with $\tilde{\Phi}(r) \sim \langle f\rangle^2$, and

(iii) S-range: $r_* \gg r \gg \eta$, with $\tilde{\Phi}(r) \gg \langle f\rangle^2$,

where $\tilde{\Phi}$ stands for either $C_{\tilde{f}}(r) = C_f(r) - \langle f\rangle^2$ or $\langle \widetilde{f_r}^2\rangle = \langle {f_r}^2\rangle - \langle f\rangle^2$ and $f = \epsilon$ or Ω.

In the DNSs with $1100 < R_\lambda < 1740$, the characteristic scale r_* is typically found to be around $0.02L$. Within the T-range, the two-point correlations C_ϵ and C_Ω, as well as the second-order moments of the local averages $\langle {\epsilon_r}^2\rangle$ and $\langle {\Omega_r}^2\rangle$, exhibit approximate power-law behavior with exponents close to 0.23. In contrast, the corresponding quantities for the fluctuation fields—$C_{\tilde{\epsilon}}$, $C_{\tilde{\Omega}}$, $\langle \widetilde{\epsilon_r}^2\rangle$, and $\langle \widetilde{\Omega_r}^2\rangle$—also exhibit approximate power-law behavior, but with steeper exponents of approximately 0.43.

In our DNSs, which reach up to $R_\lambda \approx 1740$, the width of the S-range—if it exists—appears to be too narrow to allow reliable estimation of the intermittency exponents within that range. The scaling behavior observed in the T-range should not be confused with that of the S-range, as the two presumably reflect fundamentally different regimes in terms of fluctuation intensity.

ACKNOWLEDGMENTS

The authors gratefully acknowledge P. K. Yeung and K. R. Sreenivasan for their valuable comments, which have been of great help in preparing this paper. This study used the computational resources of the supercomputer Fugaku provided by the RIKEN Center for Computational Science through the HPCI System Research Projects (Project IDs hp230143, hp240165, and hp250303). It was also supported by the Japan High Performance Computing and Networking plus Large-scale Data Analyzing and Information Systems (Project IDs jh240062 and jh250074). This research was supported by JSPS KAKENHI Grants No. JP21K11927, No. JP23K11124, and No. JP23K03245.

DATA AVAILABILITY

There are no publicly available research data or software supporting this manuscript. Requests for further information or data should be sent to the authors.

APPENDIX

1. Derivation of (27)

Substituting (27) into the definition of the spherically averaged correlation function $C_\phi(r)$ [as in (13)], we obtain

$$\begin{aligned} C_\phi(r) &= \frac{1}{4\pi r^2}\int dS_r\left[\int_0^\infty dk \int dS_k\, \widehat{C}_\phi(\mathbf{k})\exp(i\mathbf{k}\cdot\mathbf{r})\right] \\ &= \int_0^\infty dk \int dS_k\, \widehat{C}_\phi(\mathbf{k})\left[\frac{1}{4\pi r^2}\int dS_r \exp(i\mathbf{k}\cdot\mathbf{r})\right] \\ &= \int_0^\infty dk \int dS_k\, \widehat{C}_\phi(\mathbf{k})\frac{\sin(kr)}{kr} \\ &= \int_0^\infty dk\, E_\phi(k)\frac{\sin(kr)}{kr}, \end{aligned} \tag{A1}$$

where we have used (10).

2. Derivation of (33)

When the field is statistically homogeneous, i.e., when $C_\phi(\mathbf{y}, \mathbf{y}')$ depends only on the separation vector $\mathbf{y}' - \mathbf{y}$, we can write

$$C_\phi(\mathbf{x}+\mathbf{h}, \mathbf{x}+\mathbf{h}') = C_\phi(\mathbf{h}'-\mathbf{h}) = \int d\mathbf{k}\widehat{C}_\phi(\mathbf{k})\exp[i\mathbf{k}\cdot(\mathbf{h}'-\mathbf{h})], \tag{A2}$$

where $\widehat{C}_\phi(\mathbf{k})$ is the Fourier transform of $C_\phi(\mathbf{r})$.

Substituting (A2) into (33) yields

$$\begin{aligned} \langle {\phi_r}^2\rangle &= \frac{1}{V_r^2}\int_{|\mathbf{h}'|<r} d\mathbf{h}' \int_{|\mathbf{h}|<r} d\mathbf{h} \int d\mathbf{k}\, \widehat{C}_\phi(\mathbf{k})\exp[i\mathbf{k}\cdot(\mathbf{h}'-\mathbf{h})] \\ &= \frac{1}{V_r^2}\int d\mathbf{k}\, \widehat{C}_\phi(\mathbf{k})\left[\int_{|\mathbf{h}|<r} d\mathbf{h}\exp(-i\mathbf{k}\cdot\mathbf{h})\right]\left[\int_{|\mathbf{h}'|<r} d\mathbf{h}'\exp(i\mathbf{k}\cdot\mathbf{h}')\right] \\ &= \frac{1}{V_r^2}\int d\mathbf{k}\, \widehat{C}_\phi(\mathbf{k})\left[\int_{|\mathbf{h}|<r} d\mathbf{h}\exp(-i\mathbf{k}\cdot\mathbf{h})\right]^2. \end{aligned} \tag{A3}$$

The Fourier integral over a ball of radius r is known:

$$\int_{|\mathbf{h}|<r} d\mathbf{h} \exp(-i\mathbf{k}\cdot\mathbf{h}) = \frac{4\pi}{k^3}[\sin(kr) - kr\cos(kr)], \tag{A4}$$

which gives

$$\langle {\phi_r}^2 \rangle = \frac{1}{V_r^2} \int d\mathbf{k}\, \widehat{C}_\phi(\mathbf{k}) \left(\frac{4\pi}{k^3}[\sin(kr) - kr\cos(kr)] \right)^2. \tag{A5}$$

Equation (10) allows us to simplify the expression to

$$\langle {\phi_r}^2 \rangle = 9 \int_0^\infty dk\, E_\phi(k) \frac{[\sin(kr) - kr\cos(kr)]^2}{(kr)^6}. \tag{A6}$$

If one wishes to compute the locally averaged field $\phi_r(\mathbf{x})$, then it is convenient to use its Fourier transform, denoted by $\widehat{\phi_r}(\mathbf{k})$, and then apply the inverse Fourier transform (see, e.g., Aoyama *et al.* [33] and Buaria and Sreenivasan [19]). The relation between $\hat{\phi}_r(\mathbf{k})$ and $\hat{\phi}(\mathbf{k})$ is given by

$$\widehat{\phi_r}(\mathbf{k}) = \frac{4\pi}{k^3}[\sin(kr) - kr\cos(kr)]\widehat{\phi}(\mathbf{k}). \tag{A7}$$

Therefore, expression (A5) can also be derived directly from (A7).

[1] A. N. Kolmogorov, A refinement of previous hypotheses concerning the local structure of turbulence in a viscous incompressible fluid at high Reynolds number, J. Fluid Mech. **13**, 82 (1962).

[2] A. N. Kolmogorov, The local structure of turbulence in incompressible viscous fluid for very large Reynolds number, C. R. Acad. Sci. URSS **30**, 301 (1941).

[3] A. M. Oboukhov, Some specific features of atmospheric turbulence, J. Fluid Mech. **13**, 77 (1962).

[4] U. Frisch, P. L. Sulem, and M. Nelkin, A simple dynamical model of intermittent fully developed turbulence, J. Fluid Mech. **87**, 719 (1978).

[5] G. Parisi and U. Frisch, On the singularity structure of fully developed turbulence, in *Turbulence and Predictability in Geophysical Fluid Dynamics and Climate Dynamics, Proceedings of the International School of Physics Enrico Fermi, Course LXXXVIII*, edited by M. Ghil, R. Benzi, and G. Parisi (North-Holland, Amsterdam, 1985).

[6] C. Meneveau and K. R. Sreenivasan, Simple multifractal cascade model for fully developed turbulence, Phys. Rev. Lett. **59**, 1424 (1987).

[7] Z. S. She and E. Leveque, Universal scaling laws in fully developed turbulence, Phys. Rev. Lett. **72**, 336 (1994).

[8] U. Frisch, *Turbulence: The Legacy of A. N. Kolmogorov* (Cambridge University Press, Cambridge, UK, 1995).

[9] P. K. Yeung, K. R. Sreenivasan, and S. B. Pope, Effects of finite spatial and temporal resolutions on the direct numerical simulations of incompressible isotropic turbulence, Phys. Rev. Fluids **3**, 064603 (2018).

[10] N. Okamoto, T. Ishihara, M. Yokokawa, and Y. Kaneda, Effects of finite arithmetic precision on large-scale direct numerical simulation of box turbulence by spectral method, Phys. Rev. Fluids **10**, 064603 (2025).

[11] A. S. Monin and A. M. Yaglom, *Statistical Fluid Mechanics: Mechanics of Turbulence* (MIT Press, Cambridge, MA, 1975), Vol. 2.

[12] F. Anselmet, Y. Gagne, E. J. Hopfinger, and R. A. Antonia, High-order velocity structure functions in turbulent shear flows, J. Fluid Mech. **140**, 63 (1984).

[13] K. R. Sreenivasan and P. Kailasnath, An update on the intermittency exponent in turbulence, Phys. Fluids A **5**, 512 (1993).

[14] A. Praskovsky and S. Oncley, Comprehensive measurements of the intermittency exponent in high Reynolds number turbulent flows, Fluid Dyn. Res. **21**, 331 (1997).

[15] J. Cleve, M. Greiner, B. R. Pearson, and K. R. Sreenivasan, Intermittency exponent of the turbulent energy cascade, Phys. Rev. E **69**, 066316 (2004).

[16] K. P. Iyer, K. R. Sreenivasan, and P. K. Yeung, Refined similarity hypothesis using three-dimensional local averages, Phys. Rev. E **92**, 063024 (2015).

[17] J. M. Lawson, E. Bodenschatz, A. N. Knutsen, J. R. Dawson, and N. A. Worth, Direct assessment of Kolmogorov's first refined similarity hypothesis, Phys. Rev. Fluids **4**, 022601(R) (2019).

[18] P. K. Yeung and K. Ravikumar, Advancing understanding of turbulence through extreme-scale computation: Intermittency and simulations at large problem sizes, Phys. Rev. Fluids **5**, 110517 (2020).

[19] D. Buaria and K. R. Sreenivasan, Intermittency of turbulent velocity and scalar fields using three-dimensional local averaging, Phys. Rev. Fluids **7**, L072601 (2022).

[20] T. Ishihara, K. Morishita, M. Yokokawa, A. Uno, and Y. Kaneda, Energy spectrum in high-resolution direct numerical simulations of turbulence, Phys. Rev. Fluids **1**, 082403(R) (2016).

[21] T. Ishihara, Y. Kaneda, K. Morishita, M. Yokokawa, and A. Uno, Second-order velocity structure functions in direct numerical simulations of turbulence with R_λ up to 2250, Phys. Rev. Fluids **5**, 104608 (2020).

[22] P. K. Yeung and S. B. Pope, An algorithm for tracking fluid particles in numerical simulations of homogeneous turbulence, J. Comput. Phys. **79**, 373 (1988).

[23] P. K. Yeung, K. Ravikumar, R. Uma-Vaideswaran, D. L. Dotson, K. R. Sreenivasan, S. B. Pope, C. Meneveau, and S. Nichols, Small-scale properties from exascale computations of turbulence on a periodic cube, J. Fluid Mech. **1019**, R2 (2025).

[24] T. Ishihara, Y. Kaneda, M. Yokokawa, K. Itakura, and A. Uno, Spectra of energy dissipation, enstrophy and pressure by high-resolution direct numerical simulations of turbulence in a periodic box, J. Phys. Soc. Jpn. **72**, 983 (2003).

[25] Y. Kaneda and K. Morishita, Small-scale statistics, structure of turbulence–in the light of high resolution direct numerical simulation, in *Ten Chapters in Turbulence,* edited by P. A. Davidson, Y. Kaneda, and K. R. Sreenivasan (Cambridge University Press, Cambridge, UK, 2013).

[26] S. Khurshid, D. A. Donzis, and K. R. Sreenivasan, Energy spectrum in the dissipation range, Phys. Rev. Fluids **3**, 082601(R) (2018).

[27] D. Buaria and K. R. Sreenivasan, Dissipation range of the energy spectrum in high Reynolds number turbulence, Phys. Rev. Fluids **5**, 092601(R) (2020).

[28] A. Praskovsky and S. Oncley, Correlators of velocity differences and energy dissipation at very high Reynolds numbers, Europhys. Lett. **28**, 635 (1994).

[29] Y. Kaneda, T. Ishihara, M. Yokokawa, K. Itakura, and A. Uno, Energy dissipation rate and energy spectrum in high resolution direct numerical simulations of turbulence in a periodic box, Phys. Fluids **15**, L21 (2003).

[30] D. A. Donzis and K. R. Sreenivasan, The bottleneck effect and the Kolmogorov constant in isotropic turbulence, J. Fluid Mech. **657**, 171 (2010).

[31] C. Küchler, G. P. Bewley, and E. Bodenschatz, Universal velocity statistics in decaying turbulence, Phys. Rev. Lett. **131**, 024001 (2023).

[32] Y. Tsuji, Intermittency effect on energy spectrum in high-Reynolds number turbulence, Phys. Fluids **16**, L43 (2004).

[33] T. Aoyama, T. Ishihara, Y. Kaneda, M. Yokokawa, K. Itakura, and A. Uno, Statistics of energy transfer in high-resolution direct numerical simulation of turbulence in a periodic box, J. Phys. Soc. Jpn. **74**, 3202 (2005).